



# **BRNO UNIVERSITY OF TECHNOLOGY**

VYSOKÉ UČENÍ TECHNICKÉ V BRNĚ

## **FACULTY OF MECHANICAL ENGINEERING**

FAKULTA STROJNÍHO INŽENÝRSTVÍ

## **INSTITUTE OF PHYSICAL ENGINEERING**

ÚSTAV FYZIKÁLNÍHO INŽENÝRSTVÍ

## **MAGNETOTRANSPORT PROPERTIES OF FERH NANOWIRES**

MAGNETOTRANSPORTNÍ VLASTNOSTI FERH NANODRÁTŮ

### **MASTER'S THESIS**

DIPLOMOVÁ PRÁCE

#### **AUTHOR**

AUTOR PRÁCE

**Bc. Kateřina Fabianová**

#### **SUPERVISOR**

VEDOUCÍ PRÁCE

**Ing. Vojtěch Uhlíř, Ph.D.**

**BRNO 2018**



# Master's Thesis Assignment

Institut: Institute of Physical Engineering  
Student: **Bc. Kateřina Fabianová**  
Degree program: Applied Sciences in Engineering  
Branch: Physical Engineering and Nanotechnology  
Supervisor: **Ing. Vojtěch Uhlíř, Ph.D.**  
Academic year: 2017/18

As provided for by the Act No. 111/98 Coll. on higher education institutions and the BUT Study and Examination Regulations, the director of the Institute hereby assigns the following topic of Master's Thesis:

## Magnetotransport properties of FeRh nanowires

### Brief description:

Iron-Rhodium (FeRh) is a magnetic material that exhibits a phase transition from the antiferromagnetic to ferromagnetic order under the influence of temperature or magnetic field. During the phase transformation there is a significant change in electrical resistance (up to 50 %), magnetization and entropy, which suggests applications in information storage or sensors. The magnetic properties of FeRh thin films can be greatly influenced by magnetic anisotropy, which is induced by the deformation of the crystal lattice when the layer is grown on different substrates. The anisotropy of the magnetic layers can be analyzed, for example, by the magneto-optical Kerr effect. In the case of FeRh nanowires, a more suitable method consists in measuring the anisotropic magnetoresistance (AMR) dependent on the magnitude and direction of the external magnetic field. The diploma thesis will focus on the study of magnetic anisotropy related to transport properties of FeRh nanowires prepared on substrates inducing tensile or compressive strain.

### Master's Thesis goals:

1. Review the state-of-the-art.
2. Fabricate FeRh nanowires on different substrates for electrical transport measurements.
3. Carry out measurements of resistance of FeRh nanowires as a function of temperature and applied magnetic field.
4. Determine the values of anisotropic magnetoresistance in the ferromagnetic and antiferromagnetic phases of FeRh.

**Recommended bibliography:**

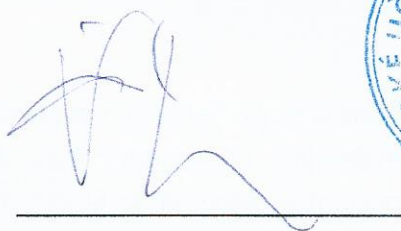
BORDEL, C. et al. , Fe Spin Reorientation across the Metamagnetic Transition in Strained FeRh Thin Films. Physical Review Letters, vol. 109, pp. 117201, DOI: 10.1103/PhysRevLett.109.117201, 2012.

McGUIRE, T. R. a POTTER, R. I., Anisotropic Magnetoresistance in Ferromagnetic 3d Alloys. IEEE Transactions on Magnetics, vol. 11, pp. 1018, DOI: 10.1109/TMAG.1975.1058782, 1976.

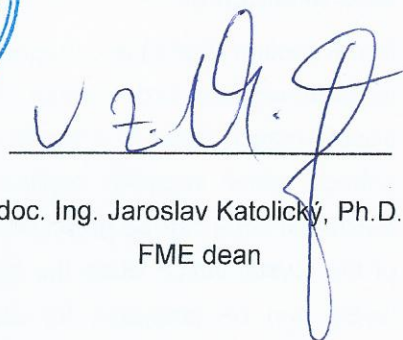
MARTI, X. et al., Room-temperature antiferromagnetic memory resistor. Nature Materials, vol. 13, pp. 367, DOI: 10.1038/NMAT3861, 2014.

Students are required to submit the thesis within the deadlines stated in the schedule of the academic year 2017/18.

In Brno, 8. 11. 2017



prof. RNDr. Tomáš Šikola, CSc.  
Director of the Institute



doc. Ing. Jaroslav Katolický, Ph.D.  
FME dean



## ABSTRACT

Iron-rhodium (FeRh) is a material undergoing a first order magnetic phase transition from antiferromagnetic (AF) to ferromagnetic (FM) phase which occurs when the material is heated above the transition temperature or by applying a sufficiently large magnetic field. This phase transition is accompanied by a significant change in entropy, magnetization and electric resistivity while the transition temperature is strongly dependent on the crystal stoichiometry, elemental substitution, pressure and in case of thin layers on the strain induced by the substrate.

This work is focused on the study of magnetotransport properties of wires patterned from FeRh thin layers grown on substrates inducing different strain in the layer. One of the main effects studied in this work is the anisotropic magnetoresistance (AMR) demonstrated by a change of the resistance for different orientations of the magnetic moments in the material with respect to the electric current direction. The AMR was studied both in the FM and AF phase of FeRh. The AMR of the FM phase in the high temperature phase was measured and an unexpected behavior of the AMR of the residual FM phase of FeRh in the low temperature phase was discovered. A strong dependence of the AMR on the orientation of the measured segment with respect to the crystallographic directions of FeRh was explored.

## KEYWORDS

iron-rhodium, phase transition, antiferromagnet, ferromagnet, transport measurement, anisotropic magnetoresistance

## ABSTRAKT

Železo-rhodium (FeRh) je látka procházející magnetickou fázovou přeměnou prvního druhu z antiferomagnetické (AF) do feromagnetické (FM) fáze, ke které dochází při zahřátí materiálu nad teplotu fázové přeměny nebo působením dostatečně velkého magnetického pole. Tato fázová přeměna je mimo jiné provázena výraznou změnou entropie, magnetizace a elektrického odporu, přičemž její tvar a poloha teploty přeměny je silně závislá na stechiometrii krystalu, na příměsích, tlaku a v případě tenkých vrstev na napjatosti vrstvy způsobené substrátem.

Tato práce se zaměřuje na studium magnetotransportních vlastností drátů připravených z tenkých FeRh vrstev rostlých na substrátech indukujících různou napjatost vrstvy. Jedním z hlavních jevů studovaných v této práci je anizotropní magnetorezistance (AMR) projevující se změnou odporu pro různé natočení magnetických momentů v látce vůči směru elektrického proudu. AMR byla studována jak ve FM fázi, tak i v AF fázi FeRh. Byla změřena hodnota AMR ve vysokoteplotní FM fázi a objeveno neočekávané chování AMR ve zbytkové FM fázi v nízkoteplotním stavu. Dále byla pozorována výrazná závislost AMR na orientaci měřených segmentů vůči krystalografickým směrům FeRh.

## KLÍČOVÁ SLOVA

Železo-rhodium, fázová přeměna, antiferomagnet, feromagnet, transportní měření, anizotropní magnetorezistance

FABIANOVÁ, K. *Magnetotransport properties of FeRh nanowires*: Brno University of Technology, Faculty of Mechanical Engineering, 2018. 66 p. Supervised by Ing. Vojtěch Uhlíř, Ph.D.



## DECLARATION

I declare that I have elaborated my master's thesis on the theme of "Magnetotransport properties of FeRh nanowires" independently, under the supervision of the master's thesis supervisor and with the use of technical literature and other sources of information which are all quoted in the thesis and detailed in the list of literature at the end of the thesis.

As the author of the master's thesis I furthermore declare that, concerning the creation of this master's thesis, I have not infringed any copyright. In particular, I have not unlawfully encroached on anyone's personal copyright and I am fully aware of the consequences in the case of breaking Regulation § 11 and the following of the Copyright Act No 121/2000 Vol., including the possible consequences of criminal law resulted from Regulation § 152 of Criminal Act No 140/1961 Vol.

.....

.....

(author's signature)



## Acknowledgement

Here I would like to thank my supervisor Ing. Vojtěch Uhlíř, Ph.D. for his guidance throughout the Master study, for the professional advice and comments and for the thorough proofreading of this thesis. I also want to thank Ing. Erik Pálesch, Ph.D. for the help with preparation of the UV mask, Ing. Marek Vaňatka for the assistance in the data processing, Dr. Ing. Michal Staňo, Ing. Lukáš Flajšman, Ing. Igor Turčan and Bc. Tomáš Martínek for the help with design and development of the new experimental setup. Further, I would like to greatly thank Mgr. Jiří Liška, Ph.D., M.Sc. Jon Ander Arregi Uribeetxebarria and Ing. Michal Horký for experimental assistance, practical tips and mental support. Special thanks go to Ing. Jakub Sadílek for help with problem solving, for the consultations and especially for being such a uplifting company for me in the last few weeks.

I would like to thank the most my partner Ing. Lukáš Kejík for the hours of reading and correcting this thesis, for his never-ending patience and tolerance of my extreme mood oscillations, for his love and support and for that he was a great companion in this episode of my life.

In the end, I would like to thank my parents, my sister and the rest of my family for their support throughout all the years of my study and for always being here for me.

This work was carried out with the support of CEITEC Nano Research Infrastructure (ID LM2015041, MEYS CR, 2016–2019), CEITEC Brno University of Technology.

Bc. Kateřina Fabianová





# CONTENTS

<b>Introduction</b>	<b>1</b>
<b>1 Basics of magnetism</b>	<b>3</b>
1.1 Magnetic fields in matter . . . . .	3
1.2 Energies in magnetism . . . . .	4
1.3 Magnetic materials . . . . .	6
1.3.1 Diamagnetic materials . . . . .	6
1.3.2 Paramagnetic materials . . . . .	7
1.3.3 Ferromagnetic materials . . . . .	8
1.3.4 Antiferromagnetic materials . . . . .	9
1.4 Magnetoresistance . . . . .	10
1.4.1 Anisotropic magnetoresistance . . . . .	10
<b>2 Iron-rhodium</b>	<b>13</b>
2.1 Phase diagram and crystal structure . . . . .	13
2.2 Magnetic phase transition in FeRh . . . . .	15
2.2.1 Influence of magnetic field . . . . .	15
2.2.2 Influence of elemental substitution . . . . .	16
2.2.3 Influence of hydrostatic pressure and strain . . . . .	17
2.3 Electric transport properties . . . . .	20
2.3.1 AMR in FeRh . . . . .	21
<b>3 Sample preparation</b>	<b>27</b>
3.1 Methods of FeRh preparation . . . . .	27
3.1.1 Deposition of FeRh thin films . . . . .	28
3.1.2 Substrates . . . . .	30
3.1.3 Capping layer . . . . .	31
3.2 Preparation of wires for transport measurement . . . . .	32
3.2.1 Etching the FeRh film . . . . .	34
<b>4 Sample characterization</b>	<b>35</b>
4.1 Vibrating sample magnetometry . . . . .	35
4.2 Magnetoresistance measurements . . . . .	37
4.2.1 Magnetoresistance measurement of FeRh nanowires . . . . .	37
4.2.2 AMR measurement of FeRh stripes . . . . .	39

<b>5</b>	<b>AMR in FeRh wires</b>	<b>43</b>
5.1	AMR in FeRh nanowires . . . . .	43
5.2	AMR in FeRh stripes . . . . .	46
5.2.1	Angular dependence of <i>AMR</i> in FeRh stripes . . . . .	48
5.2.2	Angular dependence of <i>AMR</i> - effect of stripe thickness . . . .	53
5.2.3	Angular dependence of <i>AMR</i> - effect of the W buffer layer . .	55
5.3	Discussion . . . . .	59
5.3.1	AMR of the FM phase in the high temperature state . . . . .	59
5.3.2	AMR of the FM phase in the low temperature state . . . . .	60
5.3.3	AMR of the AF phase . . . . .	61
	<b>Conclusion</b>	<b>63</b>
	<b>Bibliography</b>	<b>65</b>

# INTRODUCTION

The iron-rhodium alloy (FeRh) and its unique properties were firstly examined by M. Fallot in 1939 [1]. He discovered that FeRh with approximately equiatomic composition undergoes a first order magnetic phase transition from the antiferromagnetic (AF) phase at room temperature to the ferromagnetic (FM) phase at elevated temperature, which depends on the exact composition. In the sixties, the phase transition of the FeRh alloy was studied in its bulk form, but with the development of nanoscience, the research began to focus on the confined forms of FeRh.

Even though other materials evince this type of metamagnetic phase transition (for example  $\text{CeFe}_2\text{Ru}$ ,  $\text{Mn}_2\text{CrSb}$ ), scientists stay focused on the study of FeRh because its phase transition occurs close to the room temperature and so it is suitable for investigation of the AF-FM phase transition nature as well as applications. Throughout the years, studies of the FeRh phase transition uncovered many of its interesting properties.

During the transformation of the material from the AF to FM phase the crystal structure stays the same, only the unit cell volume slightly increases. The transition is accompanied by a change in entropy and resistivity. The resistivity decreases by almost 50 % as the electronic structure and the spin ordering changes. These effects were described and examined in detail in the past. The FeRh phase transition can be influenced by many factors like composition, crystal ordering, application of magnetic field, pressure or strain. The possibility to control the phase transition by various means makes FeRh an interesting candidate for applications like magnetic recording [2], spintronic devices [3] and magnetic refrigerators [4, 5].

The experimental part of this work is partially focused on the preparation of FeRh wires and the study of the phase transition in these structures by means of electric transport measurements. The main focus of the experimental part is concentrated on the measurements of anisotropic magnetoresistance (AMR) in the FM and AF phases. In ferromagnetic materials, the AMR effect is represented by a change of resistivity for different orientations of magnetization with respect to the direction of electric current. In antiferromagnets, a similar effect can be observed as the resistance changes with the direction of the spin axis of the AF ordering.

An overview of the nature of FeRh and its characteristic phase transition, including the state-of-the-art of its electric transport properties is presented in Chapter 2. The description of preparation of FeRh stripes on different substrates is given in Chapter 3 and the methods for characterization of the prepared layers and structures are summarized in Chapter 4. In Chapter 5, the results of AMR measurements in FeRh nanowires and stripes are presented and discussed.



# 1 BASICS OF MAGNETISM

## 1.1 Magnetic fields in matter

To describe magnetic behavior of a material, it is necessary to define quantities for description of a magnetic field. There are different ways to define these quantities and so the units and definitions of *Système international d'unité (SI)* were chosen in this thesis.

The first quantity to be described is the *magnetic field*  $\mathbf{B}$ . According to Maxwell, the  $\mathbf{B}$ -field is divergenceless and this property is expressed by the Maxwell's equation describing the Gauss's law for magnetism:

$$\nabla \cdot \mathbf{B} = 0. \quad (1.1)$$

According to this expression, non-existence of magnetic monopoles can be deduced. A divergenceless field has no sources or sinks, with all lines of force forming continuous loops [6]. The *SI* unit of the  $\mathbf{B}$  field is called tesla (symbol T), which corresponds to  $\text{kg s}^{-2} \text{A}^{-1}$ .

A different tool to describe magnetic field is the auxiliary  $\mathbf{H}$ -field, also called the *magnetic field strength* or *magnetizing force* with the unit A/m in *SI*. In free space, the relation between the  $\mathbf{B}$ -field and  $\mathbf{H}$ -field is given only by a constant called the magnetic permeability  $\mu_0$  and reads

$$\mathbf{B} = \mu_0 \mathbf{H} \text{ (in vacuum)}. \quad (1.2)$$

In a material, the contribution to the magnetic field  $\mathbf{B}$  is primarily from the auxiliary  $\mathbf{H}$ -field and secondarily from the material it self. This contribution is expressed using the magnetization vector field  $\mathbf{M}$ , which is defined as the net magnetic moment per unit volume

$$\mathbf{M} = \frac{\sum \boldsymbol{\mu}_i}{V}. \quad (1.3)$$

Its *SI* unit is the same as the one for  $\mathbf{H}$ -field (A /m). A relation between the  $\mathbf{H}$ -field and magnetization is defined using a constant called the magnetic susceptibility  $\chi$  as

$$\mathbf{M} = \chi \mathbf{H} \quad (1.4)$$

and the  $\mathbf{B}$ -field can be then expressed with it as well as

$$\mathbf{B} = \mu_0(\mathbf{H} + \mathbf{M}) = \mu_0(1 + \chi)\mathbf{H} = \mu_0\mu_r\mathbf{H} \text{ (in material)}. \quad (1.5)$$

This equation then provides an expression of relative permeability as  $\mu_r = 1 + \chi$ .

The situation for an uniformly magnetized block without any external field is illustrated in Fig. 1.1 [6]. Outside the magnet, the  $\mathbf{B}$ - and  $\mathbf{H}$ -field are identical but inside they differ significantly. In the material the  $\mathbf{H}$ -field is directed opposite both to the  $\mathbf{B}$ -field and to the magnetization  $\mathbf{M}$ , hence it is usually called the *demagnetizing field*. The  $\mathbf{H}$ -field created outside the magnet is sometimes referred to as the *stray field*.

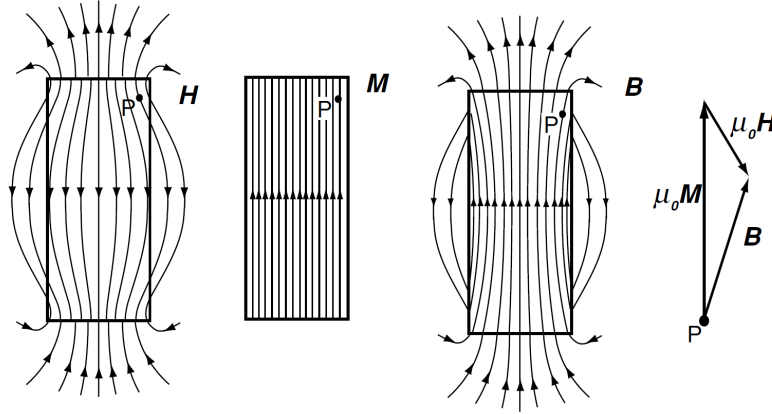


**Fig. 1.1:** Illustration of magnetic fields in a uniformly magnetized block. From the left, there is the  $\mathbf{H}$ -field, then magnetization and on the right, the  $\mathbf{B}$ -field. The  $\mathbf{H}$ -field opposes both magnetization and  $\mathbf{B}$ -field. The vector sum on the right illustrates the Eq. 1.5. Adapted from [6].

As mentioned above, existence of magnetic monopoles is in contradiction with Maxwell's equations. Nevertheless, when describing the magnetic field of a magnetic material, one can notice that the  $\mathbf{H}$ -field and magnetization  $\mathbf{M}$  do not have to be divergenceless, so we can define magnetic charges as follows

$$\rho_m = -\mu_0 \nabla \cdot \mathbf{M} = \mu_0 \nabla \cdot \mathbf{H}. \quad (1.6)$$

The possibility to choose the definition with  $\mathbf{H}$  or  $\mathbf{M}$  arises from the zero divergence of  $\mathbf{B}$  and Eq. 1.5.

## 1.2 Energies in magnetism

The stable magnetic state in a material is defined by minimization of the total free energy  $\varepsilon_{\text{tot}}$  of the system

$$\varepsilon_{\text{tot}} = \varepsilon_Z + \varepsilon_{\text{ex}} + \varepsilon_d + \varepsilon_a + \dots \quad (1.7)$$

The main contributions to the total energy are the Zeeman energy  $\varepsilon_Z$ , exchange energy  $\varepsilon_{\text{ex}}$ , dipolar energy  $\varepsilon_d$  and anisotropic energy  $\varepsilon_a$  [6, 7].



### Zeeman energy

An external magnetic field  $\mathbf{H}_{\text{app}}$  exerts a torque  $\mathbf{\Gamma} = \mu_0 \mathbf{M} \times \mathbf{H}_{\text{app}}$  on magnetization  $\mathbf{M}$ . It means that the magnetization is forced to align itself with the external field and the misalignment of the two vectors results in an energy increase expressed by the Zeeman term:

$$\varepsilon_Z = -\mu_0 \iiint_V \mathbf{M} \cdot \mathbf{H}_{\text{app}} dV. \quad (1.8)$$

### Exchange energy

The exchange interaction represents the coupling between two spins  $\mathbf{S}_i$  and  $\mathbf{S}_j$ , arising from Coulomb repulsion between the two electrons and from the Pauli exclusion principle. It covers the tendency of spins to align parallel or antiparallel and the interaction is described by the Heisenberg Hamiltonian [6, 8]:

$$\mathcal{H}_{\text{ex}} = -2 \sum_{i>j}^N J_{i,j} \mathbf{S}_i \cdot \mathbf{S}_j. \quad (1.9)$$

In this equation,  $J_{i,j}$  is the exchange constant defined by the material and its crystal symmetry. If  $J_{i,j}$  is positive, the spins will end up being parallel and the material is ferromagnetic. On the other hand, if  $J_{i,j}$  is negative, the neighbouring spins align antiparallel, which is characteristic for antiferromagnetic materials [6]. This interaction is extremely short-range and in calculations the  $J_{i,j}$  constant is usually put non-zero only for nearest neighbors.

In the approximation of continuous magnetization, the contribution of exchange interaction to the energy can be expressed using a unit magnetization vector  $\mathbf{e}_M = \mathbf{M}(\mathbf{r})/M_s$ , where  $M_s$  is the spontaneous magnetization, as

$$\varepsilon_{\text{ex}} = \iiint_V A (\nabla \mathbf{e}_M)^2 dV. \quad (1.10)$$

The constant  $A$  is called the exchange stiffness coefficient [6, 7, 9].

### Dipolar energy

The dipolar energy arises from the interaction between magnetic dipoles in a material. Every dipole creates magnetic field and contributes to the total magnetic field inside the material which is also called the *demagnetizing field*  $\mathbf{H}_d$ . The total contribution to the energy caused by this interaction can be written as [7, 9, 10]

$$\varepsilon_d = -\frac{\mu_0}{2} \iiint_V \mathbf{M} \cdot \mathbf{H}_d dV. \quad (1.11)$$

Minimization of the dipolar energy leads to reduction of magnetic charges (1.6). Although these charges are only an auxiliary concept, in many cases they can be used to simplify the description of micromagnetic problems [9]. Because the demagnetizing field strongly depends on the shape of the magnetic structure, the contribution of the dipolar interaction to the total energy is often called shape anisotropy, even though it is not related to other anisotropies described in the next section.

### Anisotropic energy

Magnetization in a magnetic material tends to align itself to certain axes (easy axes). These axes are usually linked with the crystallographic structure of the material and in that case it is caused by the magnetocrystalline anisotropy. The energy of the anisotropy depends on the orientation of magnetization with respect to the easy axis. In the case with only one easy axis, the anisotropy is called uniaxial and the simplest case of energy dependence of this arrangement can be described by the formula

$$\varepsilon_a = \iiint_V K_u \sin^2(\theta) dV \quad (1.12)$$

where  $K_u$  is the anisotropy constant and  $\theta$  is the angle between the vector of magnetization  $\mathbf{M}$  and the easy axis [7–10].

Anisotropy in a magnetic material can be influenced or induced by different factors. Such factors involve, for example, annealing the material at high temperature in a magnetic field, atomic deposition of thin films in a magnetic field or generating stress or strain in the material [6].

## 1.3 Magnetic materials

Every material can be categorized by its behavior in magnetic field. This response is described by (1.4) and based on the value of magnetic susceptibility three types of magnetic materials can be distinguished: diamagnetic, paramagnetic and ferromagnetic. However, this division is not always adequate to fully characterize magnetic properties and additional categories must be added like, for example, antiferromagnetic materials.

All magnetic materials mentioned above will be described in this section.

### 1.3.1 Diamagnetic materials

Diamagnetism is present in all materials and is caused by induction of magnetic moments with orientation opposite to the direction of the applied magnetic field (Fig. 1.2a). This behavior can be explained by the classical idea of an electron moving in a circular loop. When applying the magnetic field to a diamagnetic material,

electron is forced in a circular motion creating a magnetic field opposing the original applied field and thus weakening it. It corresponds to the induction of a electromotive force in a loop described by classical physics *Lenz's law* [10,11]. When the material is removed from the magnetic field, the induced magnetic moments vanish.

Diamagnetism is manifested by a weak negative susceptibility<sup>1</sup> which in this case does not depend on temperature. The group of materials for which the diamagnetism is the only magnetic effect are called diamagnetic.

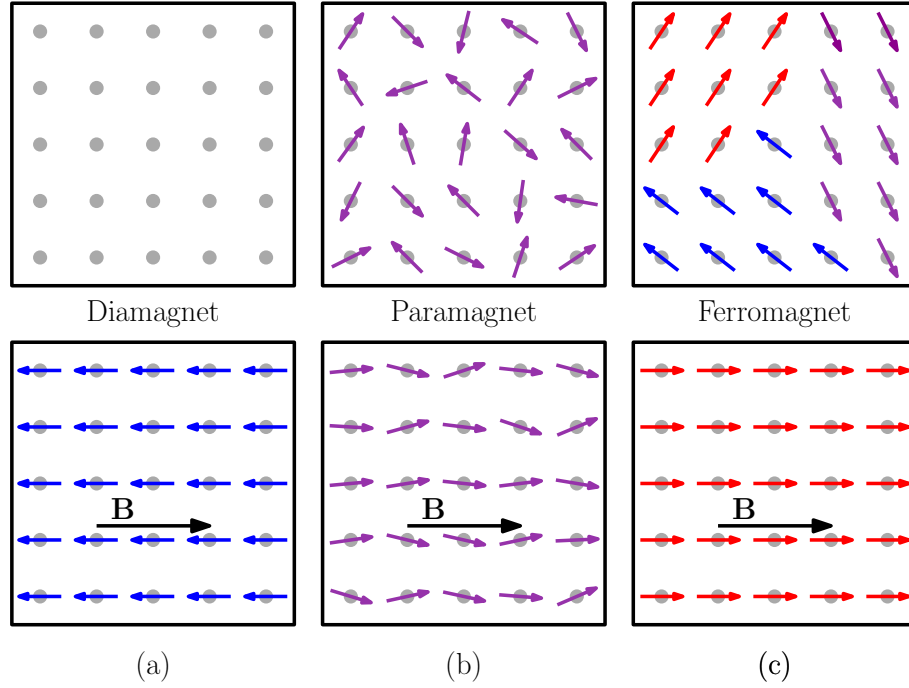


**Fig. 1.2:** Schematic representation of (a) diamagnetic, (b) paramagnetic and (c) ferromagnetic materials. In the top row, materials are depicted in the state without external field, and in the bottom row, an external magnetic field pointing to the right is applied. For schematic purposes, arrows illustrating magnetic moments are equally long, although magnetic moments of diamagnets and paramagnets are usually much smaller than those of ferromagnets.

### 1.3.2 Paramagnetic materials

Materials with non-zero magnetic moments of atoms and with weak positive susceptibility can be labeled as paramagnetic<sup>2</sup>. Magnetic moments are disordered in zero magnetic field and the resulting magnetic moment is therefore zero (magnetization is zero). When subjected to a magnetic field, magnetic moments align in the direction of magnetic field and the resulting magnetization is then non-zero (Fig. 1.2b). After removing the magnetic field, magnetic moments return to the chaotic ordering

<sup>1</sup>For diamagnetic materials the magnetic susceptibility is usually around  $\chi_d \approx -10^{-5}$ .

<sup>2</sup>For paramagnetic materials the magnetic susceptibility is usually around  $\chi_p \approx 10^{-5} - 10^{-2}$ .

and the magnetization is again zero [6, 11]. The magnetic susceptibility depends on temperature and follows a Curie law

$$\chi_p = C/T, \quad (1.13)$$

where  $C$  is the Curie constant<sup>3</sup> and  $T$  is an absolute temperature [6].

### 1.3.3 Ferromagnetic materials

A ferromagnetic material exhibits spontaneous magnetization even without an external field, i.e. magnetic moments in a certain area tend to align parallel to each other. This effect is generally caused by the exchange interaction which was explained in Section 1.2. Regions where magnetic moments are aligned in the same direction are called magnetic domains [10]. In Fig. 1.2c) different domains are apparent in the top image where no magnetic field is applied.

Important characteristic of a ferromagnet is the hysteresis loop. It is a nonlinear response of magnetization  $\mathbf{M}$  to an applied magnetic field  $\mathbf{H}$  and its typical form is depicted in Fig. 1.3. It starts at zero field with initial zero magnetization (demagnetized state). With increasing the magnetic field the magnetization increases until it reaches the value of saturation magnetization  $M_s$ . With decreasing field, the magnetization goes down but at zero field there is still some remaining magnetization which is called remanence  $M_r$ . In order to achieve zero net magnetization again, we must impose a negative field  $H_c$  called the coercive field (or coercivity). The remanence  $M_r$  and coercivity  $H_c$  depend on many factors like the sample shape, surface roughness, defects, thermal history and also on the rate at which the external field varies [6].

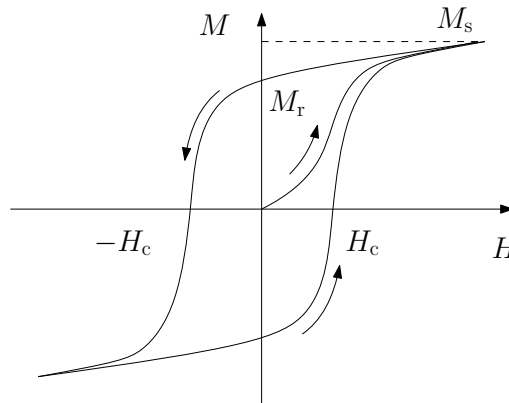


**Fig. 1.3:** Typical hysteresis loop of a ferromagnet.  $M_s$  is the saturation magnetization,  $M_r$  the remanence and  $H_c$  coercivity.

Spontaneous magnetization depends on the temperature and falls to zero when the Curie temperature  $T_C$  is reached. Above the Curie temperature, the thermal

---

<sup>3</sup> $C = n\mu_0\mu_B^2/k_B$ .

energy breaks ordering of magnetic moments in the material causing it to lose ferromagnetic properties and become paramagnetic. The dependence of susceptibility on temperature above the Curie temperature is expressed by Curie-Weiss law

$$\chi = \frac{C}{T - T_C}, \quad (1.14)$$

where  $C$  is Curie constant and  $T_C$  is Curie temperature [6].

### 1.3.4 Antiferromagnetic materials

Antiferromagnetism is another type of spin ordering in a crystal caused by the exchange interaction. With the negative exchange constant  $J$ , the neighboring magnetic moments tend to align antiparallel to each other. The crystal structure can be then described as two or more interpenetrating sublattices with spins oriented in opposite directions (Fig. 1.4). The magnetization is determined by the sum of the two sublattices and therefore the net magnetization is zero [10].

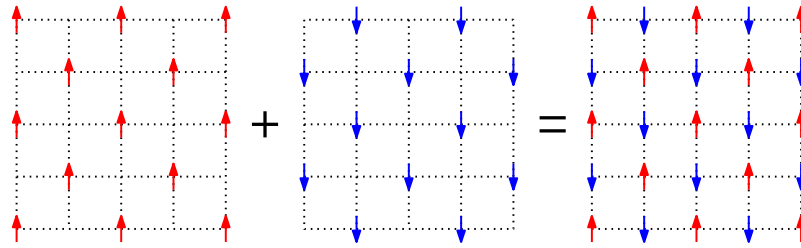


**Fig. 1.4:** Antiferromagnetic crystal is composed of two sublattices with spins oriented in opposite directions.

There are many ways to order magnetic moments in a crystal to achieve zero net magnetization. For a simple cubic structure, some examples are depicted in Fig. 1.5. The most common ordering of spins in AF materials is the type G because of its lowest exchange energy [10].

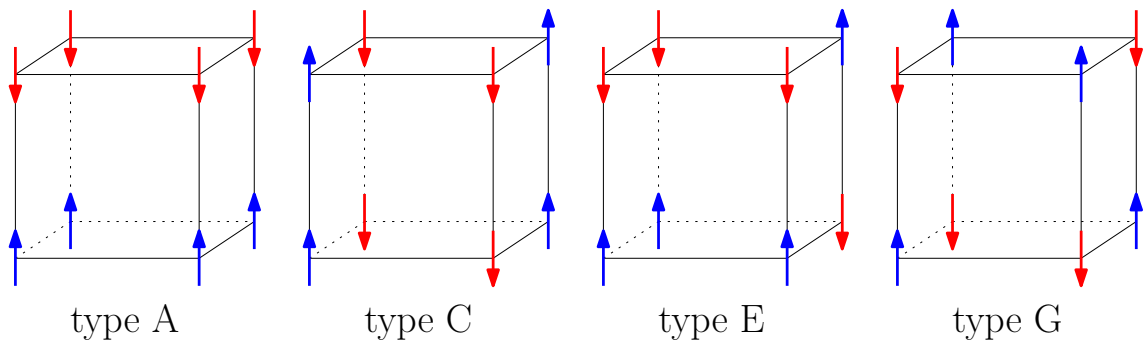


**Fig. 1.5:** Four types of antiferromagnetic ordering for a simple cubic structure.

Susceptibility of an antiferromagnet also depends on temperature. In its ordered form, the susceptibility increases until it reaches the so-called *Néel point*. Above this

point, also called Néel temperature, the material becomes paramagnetic and the temperature dependence is given by a Curie-Weiss-like law

$$\chi \propto \frac{1}{T + T_N}. \quad (1.15)$$

In Fig. 1.6, the dependence of the inverse susceptibility on temperature is drawn for paramagnetic, ferromagnetic and antiferromagnetic materials [6].

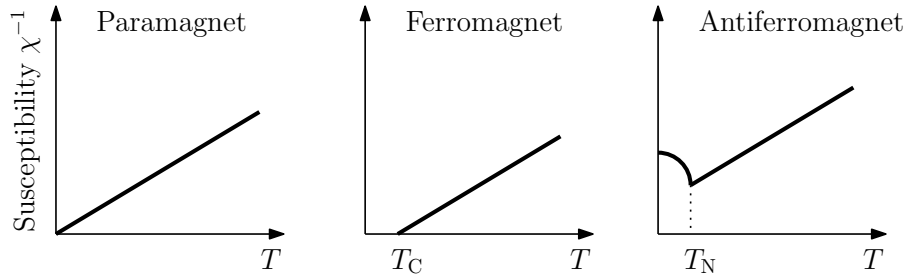


**Fig. 1.6:** Dependence of the inverse susceptibility  $\chi^{-1}$  on temperature for paramagnetic, ferromagnetic and antiferromagnetic materials. Adapted from [6].

A special category of materials exhibiting antiferromagnetic properties can be separated. These materials undergo the transformation from a antiferromagnet into ferromagnet or vice versa. The phase transition in these material can be induced by temperature or by applying a sufficiently large field which is called a metamagnetic phase transition [6]. Some materials, like iron-rhodium, undergo the phase transition from antiferromagnetic state to ferromagnetic state and during the transformation, properties like entropy, volume, magnetization and resistance change. In this work, measurements of electric resistance will be used to study the phase transition because it enables study of the examination of nanoscale structures.

## 1.4 Magnetoresistance

The change in electric resistance associated with application of an external magnetic field  $\mathbf{H}$  is called magnetoresistance (MR). One can define this effect as a relative change in resistance compared to a zero-field resistance  $R(0)$  as

$$MR = \frac{\Delta R}{R(0)} = \frac{R(\mathbf{H}) - R(0)}{R(0)}. \quad (1.16)$$

The magnetoresistance can be present also in non-magnetic materials (like *ordinary Hall effect*) or it can be associated with magnetic nature of the structure.

### 1.4.1 Anisotropic magnetoresistance

In a ferromagnet, magnetoresistance depends on relative orientation between the magnetization and the direction of electric current. This effect is known as anisotro-



pic magnetoresistance (AMR) and it is rather small (around 1 - 3 %). The resistance change is given by formula

$$R = R_{\perp} + (R_{\parallel} - R_{\perp}) \cos^2(\varphi) \quad (1.17)$$

where  $R_{\parallel}$  and  $R_{\perp}$  are resistances in the case when the magnetization and the electric current are parallel or perpendicular, respectively, and  $\varphi$  is the angle between the magnetization  $\mathbf{M}$  and the direction of electric current [12]. This dependence is illustrated in Fig. 1.7. The amplitude of relative change in resistance depends on the material and there are different ways to define the *AMR* value. One of them is written in equation

$$AMR = \frac{R_{\parallel} - R_{\perp}}{R_{\perp}}. \quad (1.18)$$

It is also possible to define *AMR* as a relative change of resistance with respect to the value in zero magnetic field which is the case, for example, in the measurement of resistance dependence on magnetic field in the hard axis direction.

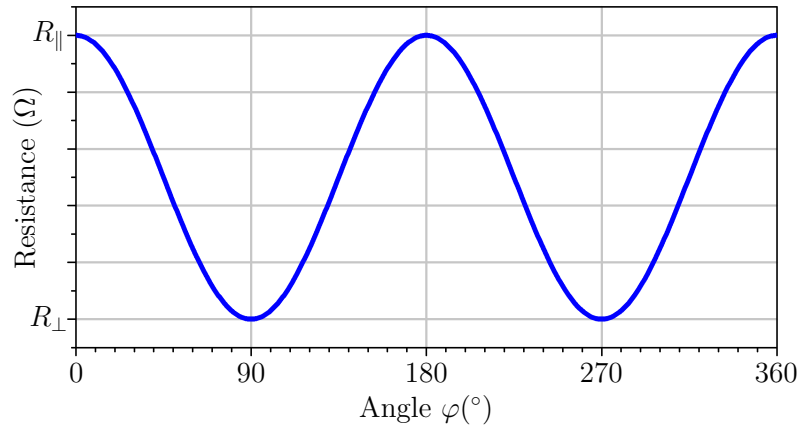


**Fig. 1.7:** Dependence of resistance of a magnetic material on the angle between the magnetization  $\mathbf{M}$  and the direction of electric current, defined as AMR.  $R_{\parallel}$  and  $R_{\perp}$  are resistances in the state where the magnetization and the current are parallel or perpendicular, respectively.



## 2 IRON-RHODIUM

Iron-Rhodium alloy (FeRh) in its near equiatomic ordered state undergoes a first-order phase transition from antiferromagnetic (AF) to ferromagnetic phase (FM) at about 370 K. Its unique properties were discovered in 1939 by M. Fallot [1] but more intense research of the FeRh system began in the sixties and continues until today [13–16].

This magnetic phase transition exhibits temperature hysteresis between heating and cooling cycles and it is accompanied by a change in magnetization, entropy, by a volume increase ( $\sim 1-2\%$ ) and by a significant drop in resistivity [17, 18]. Some of these properties will be described further in this chapter.

An interesting property of FeRh is the tunability of its transition temperature. It was shown that the temperature of the transition strongly depends on the elemental composition of the binary alloy (see Fig. 2.1) but it can be also modified by substituting iron or rhodium with different element like palladium, platinum, aluminium, nickel etc. [19–21]. The phase transition temperature can be reduced by applying magnetic field which stabilizes the FM phase [22]. Other ways to influence the phase transition will be described in section 2.2 of this chapter.

### 2.1 Phase diagram and crystal structure

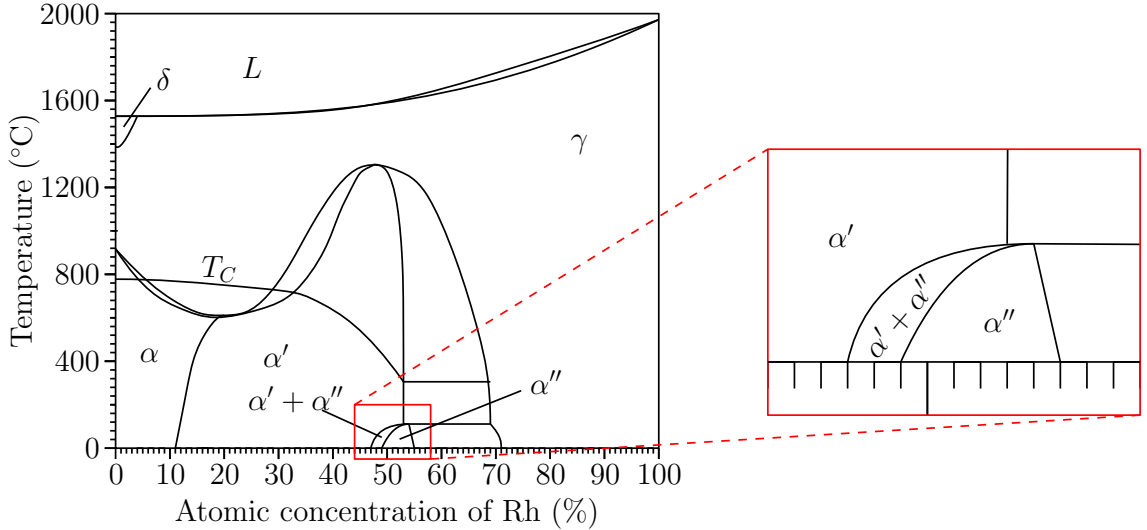


**Fig. 2.1:** Binary phase diagram of FeRh (left) and zoomed-in region of interest of the phase diagram (right):  $L$  - liquid phase;  $\gamma$  - FCC phase;  $\delta$  - high temperature BCC phase;  $\alpha$  - low temperature BCC phase;  $\alpha'$  - ferromagnetic FeRh phase with CsCl structure;  $\alpha''$  - antiferromagnetic FeRh phase with CsCl structure. Adapted from [19].

The phase transition from the AF phase to FM phase occurs only in a narrow interval of Rh concentration ( $\sim 48-54\%$ ). The binary phase diagram of bulk FeRh

was proposed in 1984 by Swartzendruber [19] and is shown in Fig. 2.1, where the  $\alpha''$  phase is the AF phase of FeRh. With increasing temperature, the phase transition is observed and the alloy transforms into the FM phase ( $\alpha'$ ). The transition temperature  $T_t$  is strongly dependent on the respective concentrations of Fe and Rh. Further, as the temperature increases, it reaches the Curie temperature ( $T_C \approx 700$ -800 K) and the material undergoes second-order transition to the paramagnetic phase. The phase diagram of the FeRh alloy was also proposed by Kubaschewski [23] in 1982 and the region of Rh content with the AF-FM transition was studied by Inoue [24].

The crystal structure of both AF and FM phases of FeRh is simple cubic with a primitive cell composed of two atoms (iron in the 000 position and rhodium in the  $\frac{1}{2}\frac{1}{2}\frac{1}{2}$  position). In other words, there are two interpenetrating simple cubic lattices, where the corner of one cell is in the body center of the other (Fig. 2.2). This arrangement is called the CsCl structure and sometimes it is described as body-centered cubic structure (BCC) because of their similar appearance.

Even though FeRh is in both AF and FM phases of CsCl crystal structure, they differ slightly in the lattice parameter. In the AF phase the lattice parameter is  $a = 2.985 \text{ \AA}$  and as the FeRh undergoes the phase transition, the crystal expands and the lattice parameter expands to  $3.000 \text{ \AA}$  [15].

Concerning the magnetic properties of the crystal, the AF phase ordering is the G type, which means that magnetic moments of nearest-neighbor Fe atoms are antiparallel and the planes with the same orientation of spins are those with (111) orientation. The magnetic moment of Fe atoms in this conformation is  $\mu_{Fe} = 3.3\mu_B$  and Rh atoms do not have any magnetic moment. In the FM phase the magnetic moments of Fe atoms are parallel with  $\mu_{Fe} = 3.2\mu_B$  and the created field induces a magnetic moment of  $\mu_{Rh} = 0.9\mu_B$  in Rh atoms [14, 25]. These two orderings are depicted in Fig. 2.2.

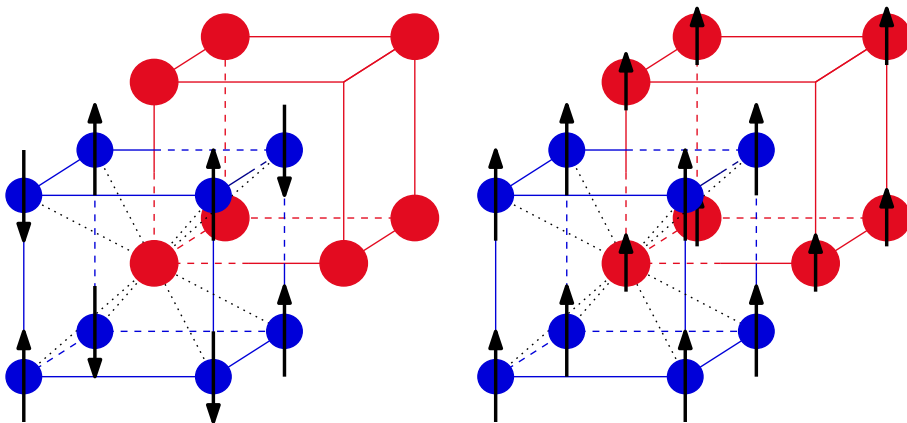


**Fig. 2.2:** Crystal structure of near equiatomic FeRh system in the AF (left) and FM (right) phase. Iron and rhodium atoms are represented by blue and red spheres, respectively.

## 2.2 Magnetic phase transition in FeRh

Transformation of FeRh from the AF to FM phase represents a first-order magnetic phase transition. This type of transition is characterized by an abrupt change in ordering and coexistence of the two phases in the middle of the transition, which is illustrated in the zoomed-in phase diagram of FeRh as the  $\alpha' + \alpha''$  phase (Fig. 2.1). The transition from FM to paramagnetic phase is continuous, i.e. the change in magnetization is gradual and the two phases cannot be distinguished at the transition temperature, the so-called critical point. This type of transformation is called the second-order phase transition [26, 27].

The transition temperature from AF to FM phase is strongly dependent on many factors including the ratio of Fe and Rh atoms, elemental substitution, magnetic field, electric current, pressure and strain induced by the substrate.

### 2.2.1 Influence of magnetic field

Magnetic field influences the phase transition by stabilizing the FM phase in FeRh, which leads to a decrease in the transition temperature. In 1966, J. S. Kouvel [20] studied the influence of doping the *bulk* FeRh by palladium, platinum and iridium on the transition temperature and observed also the field dependence of the transition temperature. Table 2.1 shows his experimental results. For pure FeRh, he found that the magnetic field reduces the transition temperature by  $-8.2$  K/T and that different elements mixed in FeRh can reduce or increase the influence of the magnetic field on the phase transition.

**Tab. 2.1:** Transition temperature and its shift by magnetic field for bulk FeRh with elemental substitution  $\text{Fe}(\text{Rh}_{1-x}\text{M}_x)_{1.08}$ . Adapted from [20].

M	...	Pd	Pd	Pt	Ir	Ir	Ir
$x$	0	0.029	0.058	0.056	0.056	0.084	0.121
$T_{\text{crit}}$ (K)	328	252	169	403	499	545	585
$\partial T_{\text{crit}}/\partial B$ (K/T)	-8.2	-11.8	-16.9	-7.3	-5.2	-4.9	-2.6

The influence of magnetic field in *thin films* grown on single-crystal MgO and sapphire substrates was studied by S. Maat et al. [22]. They measured the temperature dependence of magnetization for different magnetic fields by VSM (vibrating sample magnetometry). They confirmed that magnetic field stabilizes the FM phase and, therefore, reduces the transition temperature. They also investigated the temperature dependence of the remanent magnetization. Figs. 2.3a) and b) show the observed temperature dependence. The phase transition is shifted to lower temperatures when the magnetic field is applied. Figs. 2.3c) and d) show the temperature dependence of remanent magnetization during heating and cooling, respectively,

which reveals the irreversibility of field-induced magnetization changes during heating but their reversibility during cooling. A  $T(B)$  phase diagram can be established from the temperature dependence of magnetization in constant magnetic fields and from the field dependence at constant temperatures (Fig. 2.4). From this phase diagram, one can calculate the field shift of the phase transition  $\partial T/\partial B \approx -8 \text{ K/T}$  for FeRh on MgO single-crystal substrate, which is in a good agreement with bulk FeRh [20].

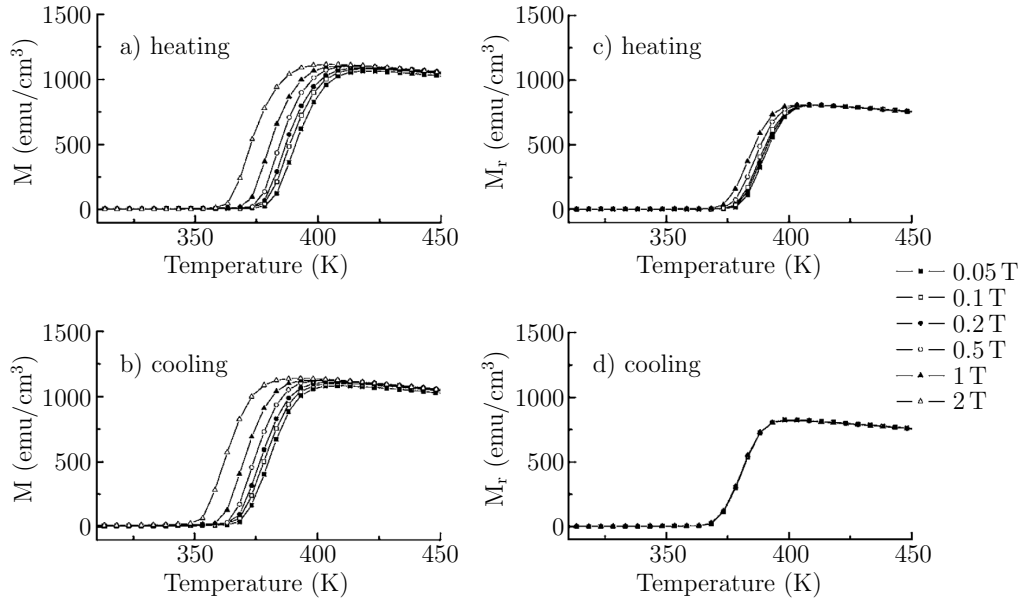


**Fig. 2.3:** Dependence of magnetization (left) and remanence (right) on temperature of FeRh *layer* grown on MgO single-crystal substrate during heating (top) and cooling (bottom) in the presence of various external magnetic fields. Adapted from [22].

### 2.2.2 Influence of elemental substitution

In 1966, J. S. Kouvel [20] observed that substituting atoms of rhodium in *bulk* FeRh alloy may result in a change of the magnetic phase transition temperature. He studied the influence of palladium, platinum and iridium doping on the transition. He focused on the variation of the entropy change during the transition, the magnetization change and the transition temperature shift (by means of doping and applying the magnetic field). In Table 2.1, the influence of doping and magnetic field is displayed. His results show that doping FeRh with palladium decreases the transition temperature significantly while doping it with platinum or iridium shifts the transition to higher temperatures.

An in-depth study of elemental substitution in FeRh was led by R. Barua [21] in 2013 with a goal to predict the magnetostructural trends in FeRh ternary systems. In that study, they linked the transition temperature to the average weighted valence



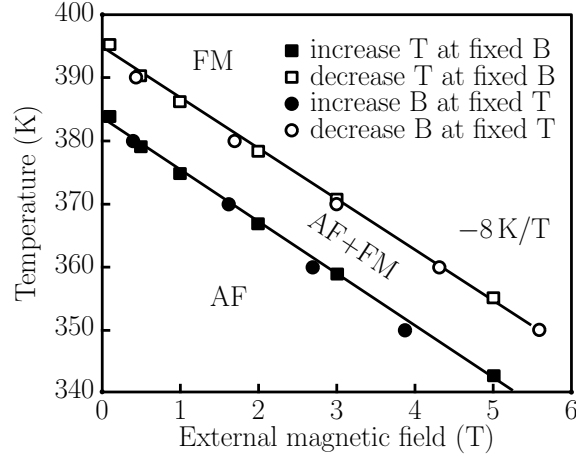


**Fig. 2.4:**  $T(B)$  phase diagram for FeRh *layers* on MgO single-crystal substrate. Shift of the transition temperature caused by external magnetic field is  $-8 \text{ K/T}$ . Adapted from [22].

band electron concentration and created a phenomenological model to predict the doping influence. They gathered results from previous studies concerning doping FeRh with another element and represented their influence on the phase transition in the periodic table (Fig. 2.5). Their conclusion was that substitution with a 3d transition metal results in a transition temperature decrease and substitution with a 5d transition metal results in an increase. No obvious trend was found for doping with 4d transition metals.

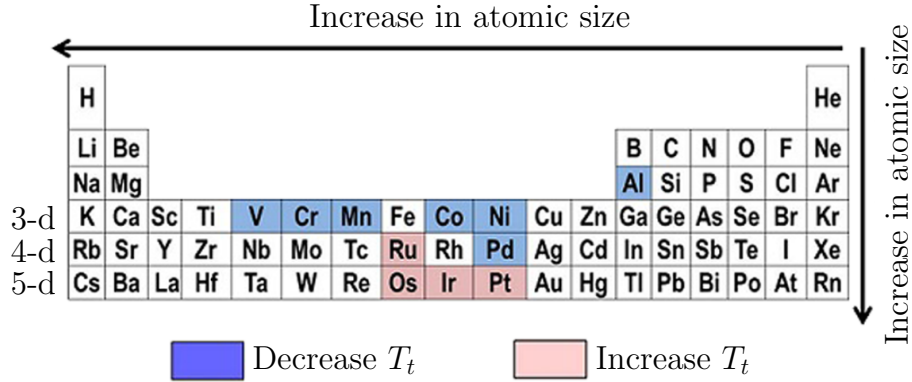


**Fig. 2.5:** Periodic table summarizing the influence of doping on the phase transition temperature  $T_t$ . Adapted from [21].

### 2.2.3 Influence of hydrostatic pressure and strain

As mentioned above, the FM and AF phase of FeRh have the same crystallographic structure with a different lattice parameter. The FM phase lattice parameter is slightly larger than the AF one [15]. Therefore, if the lattice is subjected to some

external force, the magnetic properties of the material can change. The change in the lattice parameter can either give preference to the AF phase or to the FM phase.

The influence of hydrostatic pressure on the phase transition in *bulk* FeRh alloy was studied in 1966 by A. I. Zakharov [15]. The phase transition was examined for different pressures applied on FeRh and a linear trend of the transition temperature was observed with a slope of 4.27 K/kbar. R. C. Wayne who studied the influence of tensile pressure found a decreasing linear trend with a slope of  $-2$  K/kbar [16].

In FeRh *thin films*, the crystal lattice is influenced by the substrate structure. Especially in the epitaxially grown layers, the misfit strain causes distortion of the lattice. MgO (001) and  $\text{Al}_2\text{O}_3$  (0001) (sapphire) are two examples of substrates for epitaxial growth of FeRh thin layers with orientations (001) and (111), respectively.

The strain effect of these two substrates on FeRh layer was investigated in 2005 by S. Maat et al. [22]. The determined in-plane (IP) and out-of-plane (OOP) lattice constants and strain parameters at room temperature are summarized in Table 2.2. It is apparent that the MgO substrate causes a slight expansion OOP and a compression IP in the FeRh layer (tetragonal distortion). The sapphire substrate compresses the layer in the OOP direction and expands it in the IP direction. The volume of the FeRh unit cell is about the same on both substrates. They showed that stabilization of the FM phase on the sapphire substrate can be expected as it is easier for the lattice to expand in the OOP direction. The comparison of magnetization versus temperature curves for FeRh on MgO and sapphire is represented in Fig. 2.6. It shows that the phase transition of FeRh on sapphire takes place at lower temperature than in the case of the MgO substrate.

**Tab. 2.2:** Lattice and strain parameters of FeRh *films* grown on MgO (001) and sapphire (0001) along certain crystallographic directions. The strain values are derived from the experimental lattice parameter of  $2.988 \text{ \AA}$ . Reproduced from [22].

FeRh/MgO	FeRh/sapphire	$\Psi$	$a$ ( $\text{\AA}$ )	Strain (%)	$a$ ( $\text{\AA}$ )	Strain (%)
		( $^\circ$ )	MgO	MgO	sapphire	sapphire
(002)	(111)	0.0	2.9980	+0.33	2.9800	-0.27
	(110)	35.2			2.9854	-0.09
(011)		45.0	0.9890	+0.03		
	(200)	54.7			2.9901	+0.07
(020)	(1-10)	90.0	2.9750	-0.44	2.9950	+0.23

Other examples of substrates for epitaxial growth of FeRh are  $\text{SrTiO}_3$  (STO) and  $\text{KTaO}_3$  (KTO). The strain effect of these two substrates and MgO on various FeRh *thin film* thicknesses was investigated by A. Ceballos [28] in 2017. MgO, KTO and STO substrates with effective lattice parameters  $2.981 \text{ \AA}$ ,  $2.821 \text{ \AA}$  and  $2.761 \text{ \AA}$ , respectively, induce tensile strain in the FeRh films. They examined the dependence of the transition temperature and width of the transition on the thickness of the

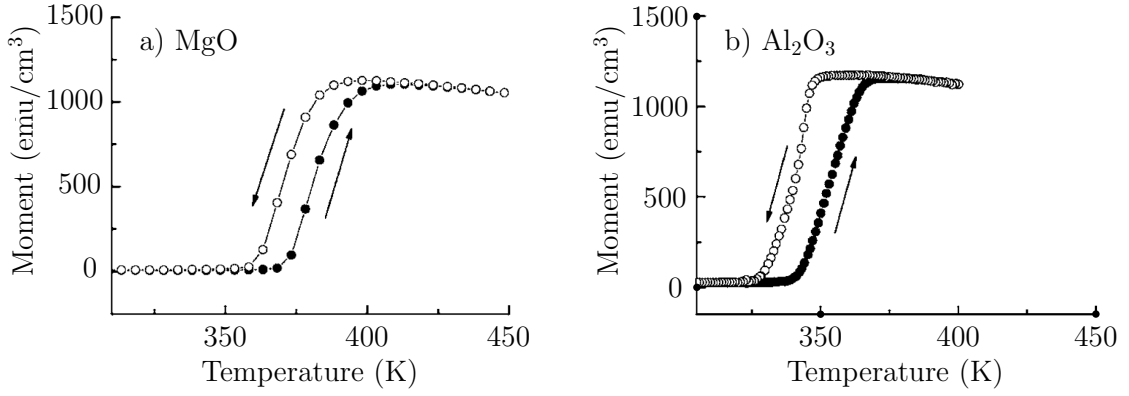


**Fig. 2.6:** Dependence of magnetization on temperature for epitaxial layers of FeRh on a) MgO and on b) sapphire. Adapted from [22].

FeRh layer and the trends are represented in Fig. 2.7. One can see, that for films under 20 nm thickness, the transition temperature abruptly decreases and the width of the transition increases. They also studied the effect of the strain in FeRh films grown onto high energy ion-beam-assist-deposited MgO (IBAD MgO), which produces a significant tensile strain [29].

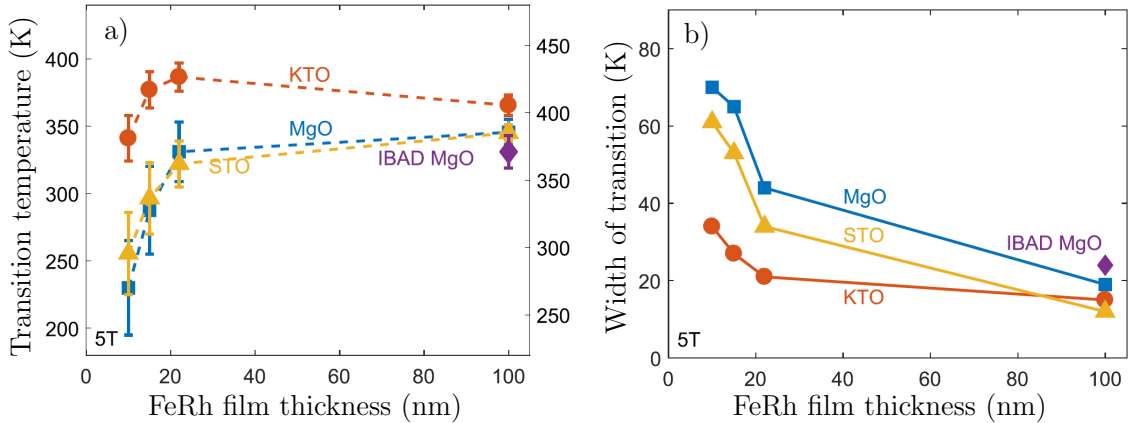


**Fig. 2.7:** Dependence of a) transition temperature and of b) width of the transition on FeRh film thickness for different substrates. Adapted from [28].

R. O. Cherifi [30] and Y. Lee [31] investigated the possibility to modulate and control the AF-FM phase transition in epitaxially grown FeRh *films* on ferroelectric substrates BaTiO<sub>3</sub> and PMN-PT<sup>1</sup>, respectively, by applying the electric field to the substrate. The electric field in these piezoelectric substrates causes a deformation of the substrate and by this means it induces strain in the FeRh layer dependent on the applied voltage.

The tungsten crystal is another substrate which can be used for epitaxial deposition of FeRh layers. Its 3.1652 Å lattice parameter [32] is slightly larger than

<sup>1</sup>Lead Magnesium Niobate-Lead Titanate - (1-x)Pb(Mg<sub>1/3</sub>Nb<sub>2/3</sub>)O<sub>3</sub>-xPbTiO<sub>3</sub>

the FeRh one. The lattice mismatch favors the FeRh FM phase which has a larger lattice constant than the AF phase and therefore induces tensile strain and shifts the phase transition to lower temperatures [33, 34]. Its BCC crystal structure suggests the possibility of tungsten epitaxial growth on MgO substrate and subsequent deposition of FeRh layer. This procedure was investigated by R. Witte [35] in 2016 and with carefully chosen growth conditions (50 nm of W and 13 nm of FeRh) they observed a collapse of magnetic structure by means of unexpected crystallographic transformation. The strain in FeRh induced by the tungsten buffer layer causes a tetragonal distortion of the FeRh lattice and in this case, it induces a tetragonal-to-orthorhombic transition. This process caused by lattice instability is called martensitic transformation. The FeRh layer did not show any AF-FM phase transition and the magnetic ordering was completely broken down by the structural change.

## 2.3 Electric transport properties

The FeRh phase transition is accompanied by an abrupt change in resistivity which has a direct connection to the magnetic ordering [17, 18, 36–38]. Below as well as above the transition temperature, the FeRh exhibits usual metallic behavior. The significant drop in resistivity during the heating cycle can reach up to 50 % magnitude. The transition from the AF to FM phase also induces a volume change of about 1-2 % but this change of geometry itself cannot explain the huge resistivity change. In Fig. 2.8, an example of the measurement of magnetization and resistivity of a FeRh *layer* grown on MgO single-crystal substrate is displayed. The shift of the phase transition temperature due to the magnetic field is also demonstrated.

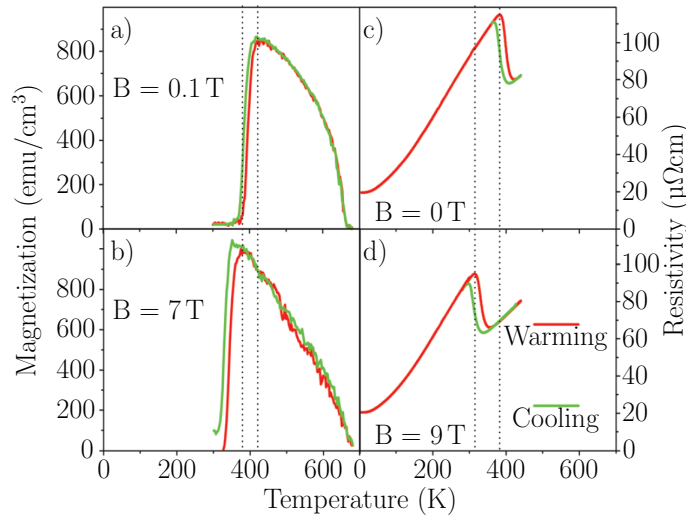


**Fig. 2.8:** Dependence of magnetization on temperature measured at a) 0.1 T and b) 7 T and resistivity on temperature measured at c) 0 T and d) 9 T for FeRh 100-nm-thick *thin films* grown on MgO single-crystal substrate. Adapted from [38].

The phase transition in FeRh thin films is strongly influenced by the nature of the substrate. Further restriction in dimensions revealed an unexpected asymmetry of the phase transition during heating and cooling. This behavior was studied by V. Uhlíř [39] et al. by resistance measurements of FeRh stripes with submicron width. They found that during the transition from the AF to FM phase, the resistance change is smooth, similar to that observed in thin films, but during the transition from the FM to AF, the transition proceeds through a few large steps in resistance (Fig. 2.9). They explain this behavior by different character of the FM and AF exchange interaction in the presence of disorder. The size of AF domains is strongly limited by the impurities and defects, but for the FM interaction these inhomogeneities do not play a significant role. This difference causes different amount of nucleation centers during the AF-FM and FM-AF transitions.

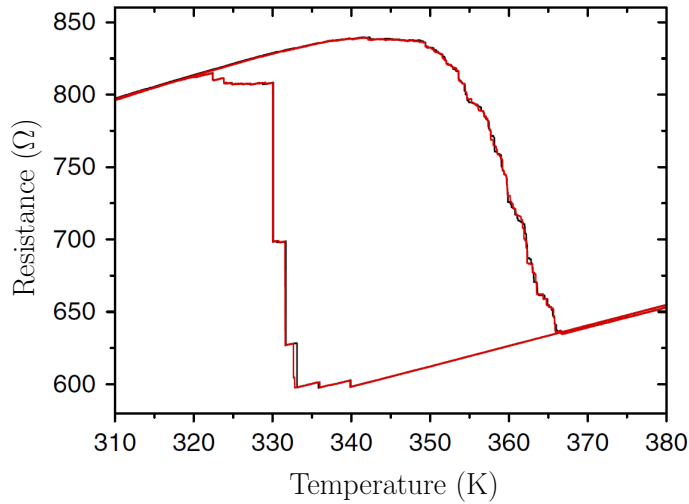


**Fig. 2.9:** Resistivity as a function of temperature representing the staircase-like behavior of the FeRh AF-FM phase transition and the almost smooth resistivity dependence during the FM-AF transition in submicron-wide FeRh stripes. Adapted from [39].

### 2.3.1 AMR in FeRh

Anisotropic magnetoresistance in ferromagnetic materials is a well-known phenomenon, which is also present in the FeRh FM phase. M. Sharma et al. [38] studied magnetotransport properties of 100 nm FeRh *film* grown on MgO single-crystal substrate. One of the studied properties was the AMR of the FM phase at different temperatures through the phase transition.

The AMR effect in the FeRh *film* was measured using van der Pauw geometry. Figs. 2.10a) and b) show the AMR determined by measuring the dependence of resistivity on low magnetic field applied in two directions, either with the magnetic field aligned with the current flow (Fig. 2.10a)) or perpendicular to it (Figs 2.10b)).

In both configurations, the field is applied in-plane. They define  $AMR$  as a relative change with respect to the high magnetic field value  $[\rho(B) - \rho(0.5 \text{ T})]/\rho(0.5 \text{ T})$ . Fig. 2.10c) shows the temperature dependence of the  $AMR$  amplitude for the two configurations throughout a sequential cooling. The phase transition is marked by two dotted lines. During the phase transition from the FM to AF phase, the  $AMR$  decreases as the volume of the FM phase in the layer decreases. The maximum  $AMR$  amplitude of the FM phase was determined to be approximately 0.45 %.

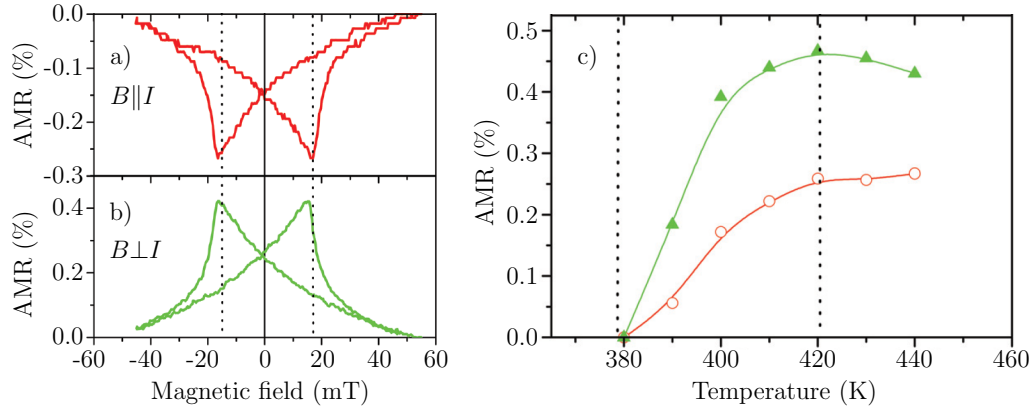


**Fig. 2.10:**  $AMR$  measured in van der Pauw configuration in the FeRh *thin film* for the FM phase at 440 K with orientation of the magnetic field a) parallel and b) perpendicular to the current flow. c) The dependence of  $AMR$  on temperature. Adapted from [38].

In 2014, X. Marti et al. [3] measured a similar effect to AMR in ferromagnets in the AF phase of FeRh. Because the AMR is an even function of the microscopic magnetic moment vector, its effect is determined only by the spin axis orientation with respect to the current. This gave rise to the assumption, that the AMR effect could be present also in antiferromagnets.

The difficulty of studying the effect of spin axis orientation with respect to the electrical current in the AF phase is that the AF-coupled spins do not typically reorient with the magnetic field. Therefore, Marti used the phase transition from the FM to AF phase in FeRh to define the orientation of the spin axis of the AF phase. By applying a magnetic field at temperatures above the AF-FM transition, the magnetic moments in the FM phase reorient in the direction of the field. By reducing the temperature, the FeRh undergoes the transition to the AF phase and the applied magnetic field forces the staggered spin moments of the AF to get oriented in the direction perpendicular to the external magnetic field (Fig. 2.11). Due to the shape anisotropy in the FeRh thin layer, the spins get oriented in the in-plane direction. The resulting orientation was confirmed by X-ray magnetic linear dichroism (XMLD).

Using this method, the spin axis of the FeRh AF phase was oriented parallel and perpendicular to the injected current. The experiment was repeated several times and the resistances of the two states were stable and reproducible (Figs. 2.12a)

and b)). The stability in magnetic field and distinguishability of the two states at different orientation and intensity of the field is shown in Fig. 2.12c) and 2.12d). In Fig. 2.12d), the variation in the resistance signal is due to the AMR associated with the residual FM phase confined at the interface with the substrate [40].

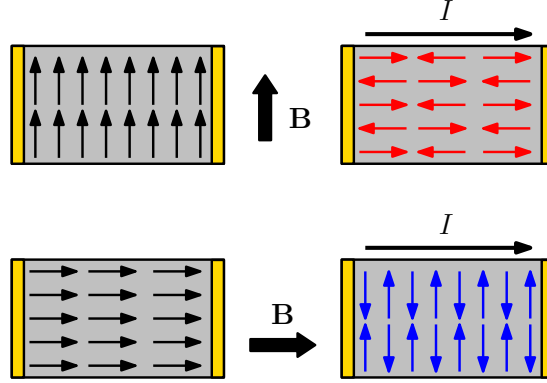


**Fig. 2.11:** Scheme of the process of ordering the AF phase in the FeRh film when transitioning from the FM phase. Magnetic field is applied in a certain direction during the phase transition from FM to AF, which causes the staggered spins in the AF phase to align in the direction perpendicular to the applied field. Adapted from [3].

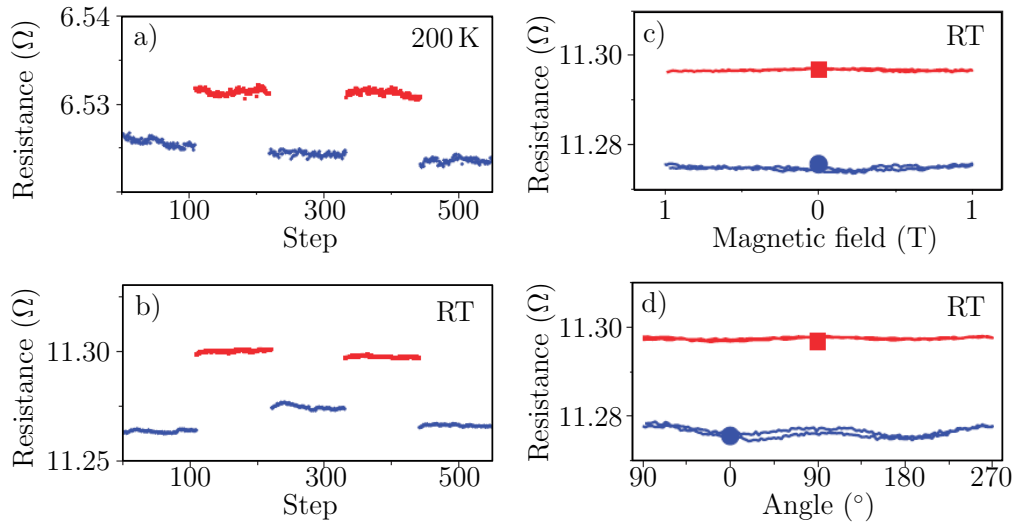


**Fig. 2.12:** Results of the AMR measured in AF phase at a) 200 K and at b) room temperature. The stability and distinguishability tests of the two states on a magnetic field at room temperature upon changing c) the intensity of magnetic field along the direction of current and d) the orientation of the 1 T applied magnetic field. The red curves correspond to the AF phase axis aligned parallel to the current and blue curves correspond to the AF phase axis aligned perpendicular to the current. Adapted from [3].

In 2015, T. Moriyama et al. [41] presented their study (based on Marti's publication [3]) of sequential write-read operations in AF antiferromagnetic phase. In the experiment, the phase transition of FeRh from the AF to FM phase is induced by applied electric current, which increases the temperature of the FeRh wire by Joule heat. The characteristic resistance drop indicating the phase transition induced by electric current is plotted in Fig. 2.13. The AMR in the AF phase is detected by measuring the resistivity of wires patterned into a cross configuration displayed in Fig. 2.14a). Using field cooling in two orthogonal directions of magnetic field, the AF spin axis is stabilized in two perpendicular orientations as shown in Figs. 2.14b) and c). By measuring the change  $\delta$  in the ratio  $R/R_{ref}$  (see Fig. 2.14) for the two AF states, the AF AMR can be determined as the resistance difference  $\Delta R = R_{\parallel} - R_{\perp}$  as  $\Delta R = R_{ref}\delta/2$ . Although the AMR value determined from their measurement is rather small compared to Ref [3], the two states of ordering of the AF phase are sharply separated (Fig. 2.15).

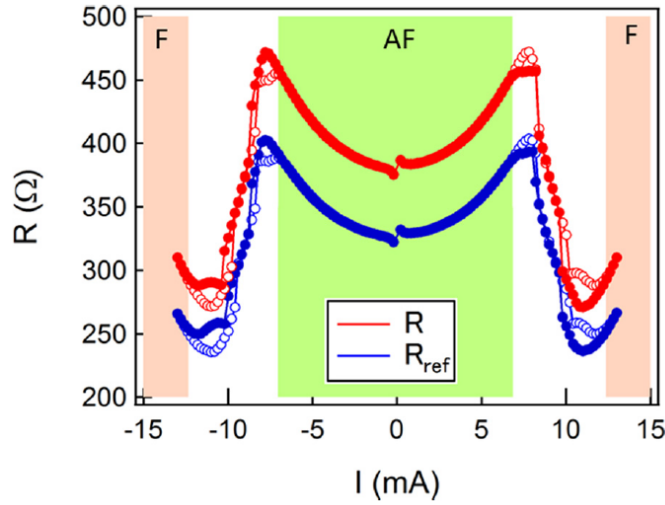


**Fig. 2.13:** Resistance of the FeRh wire dependent on the applied current. The Joule heat created by electric current heats the wire which undergoes the phase transition. Regions of the AF and FM (F) phases are indicated by green and red colors, respectively. Adapted from [41].



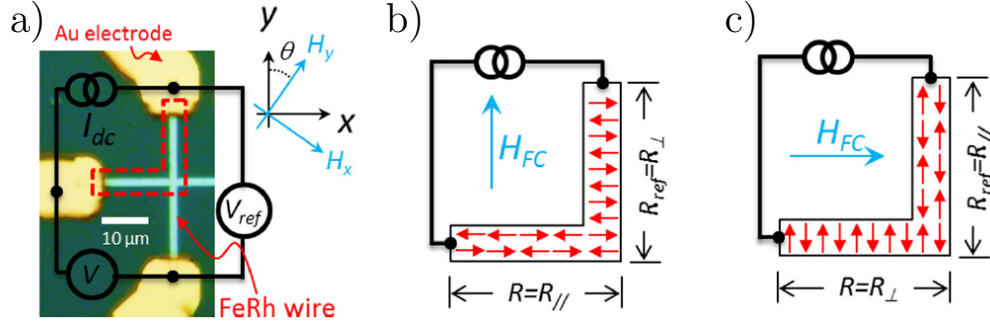


**Fig. 2.14:** a) Scheme of the measured cross-wire setup. The path of the applied current and the measured voltages  $V$  and  $V_{ref}$  are indicated. b) and c) scheme of the AF ordering inside the wire for magnetic field applied in the  $y$  direction and  $x$  direction, respectively. Adapted from [41].

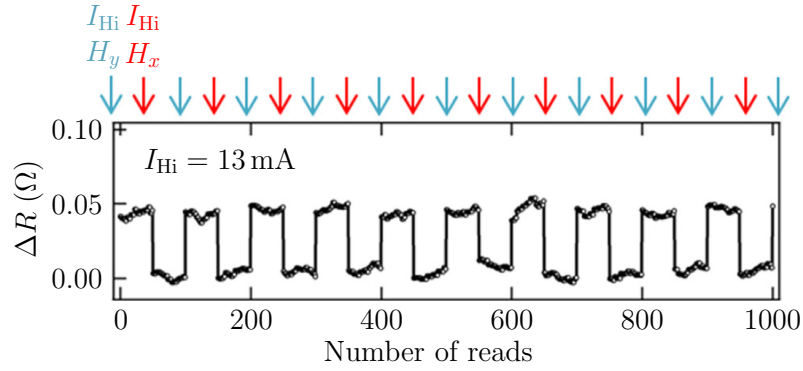


**Fig. 2.15:** Sequential read and write process in the AF phase of FeRh demonstrated by the resistance change as a function of number of reads. Prior to each read process,  $I_{Hi}$  is sent through the wire and magnetic field  $H_y$  or  $H_x$  of intensity 0.3 T is applied in the  $y$  or  $x$  direction, respectively. Then the current is reduced, the magnetic field is removed and the resistance is recorded. Adapted from [41].



## 3 SAMPLE PREPARATION

### 3.1 Methods of FeRh preparation

The phase transition from the AF to FM phase in FeRh is strongly dependent on the composition of the material and on its crystal form. Bulk FeRh is usually prepared by melting Fe and Rh together and then cooling it down. In 1968, R. C. Wayne [16] studied the influence of FeRh thermal treatment on its phase transition and found that the way the material is cooled down strongly influences the behavior of the phase transition. After annealing the material at high temperature, he either cooled it slowly down to room temperature or he employed a fast water quench by which he had achieved more reproducible results.

For the preparation of FeRh layers, different approaches can be applied. The first study of FeRh thin layers were carried out by J. M. Lommel [42]. In his article, he describes three methods to prepare FeRh thin layers. In the first method, he alternately deposited layers of Fe and Rh using electron beam melting. During the deposition, the substrate was held at 300 °C and subsequently it was heated up to 565 °C for 4 hours to promote diffusion between layers. The second preparation method comprised of co-deposition of Fe and Rh by evaporation, while the substrate was held at 300 °C. In the third method, FeRh was sputtered from alloy targets of 50 at. % Rh and 54 at. % Rh onto substrates heated again to 300 °C. No further annealing was performed in the second and third method. Lommel summarizes, that with the first method he is able to achieve a phase transition with broad temperature hysteresis, but with the second and third one partial or no transition was observed.

Further research of FeRh thin layer preparation shows that the annealing process after deposition is very crucial for the phase transition appearance and the Lommel's second and third methods give better results if the layer is annealed after the deposition. In 1999, J. van Driel et al. [18] observed that the process of annealing is very important for the transformation of a layer to the ordered CsCl-type FeRh phase. They prepared their layers by co-evaporation of Fe and Rh and subsequently annealed it using different annealing protocols. Comparison of magnetization curves as a function of temperature for FeRh annealed at different temperatures can be seen in Fig. 3.1. The sharpest and narrowest phase transition was achieved when annealing at 720 K.

Generally in literature, the process of preparation of ordered FeRh layers with phase transition differs but for the best results in terms of width and completeness of the transition, deposition at elevated temperature and annealing at even higher temperature are used [2,22,29–31,33]. The specific preparation process of FeRh thin films for the purpose of this study is described in Section 3.1.1.

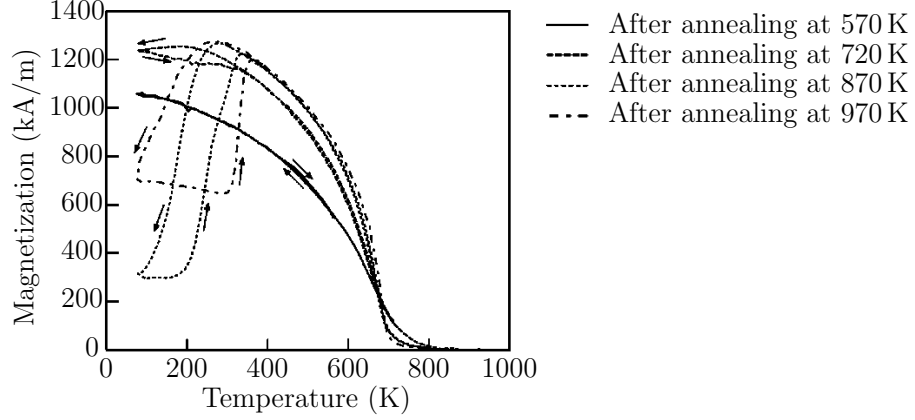


**Fig. 3.1:** Magnetization as a function of temperature for samples annealed at different temperatures. Adapted from [18].

### 3.1.1 Deposition of FeRh thin films

In this work, we use magnetron sputtering for deposition of FeRh layers. It is a physical vapor deposition method (PVD) where the source of sputtered particles is a magnetron gun [43]. The argon gas is delivered towards the target and it is ionized by a DC voltage creating plasma. The plasma is maintained near the target surface in a more condensed state and the present charged particles sputter the target material [44]. The magnetron contains a permanent magnet which creates magnetic field above the target and confines the charged particles, increasing the efficiency of the sputtering process. Sputtered atoms then exit the magnetron and travel towards the substrate (Fig. 3.2a)).

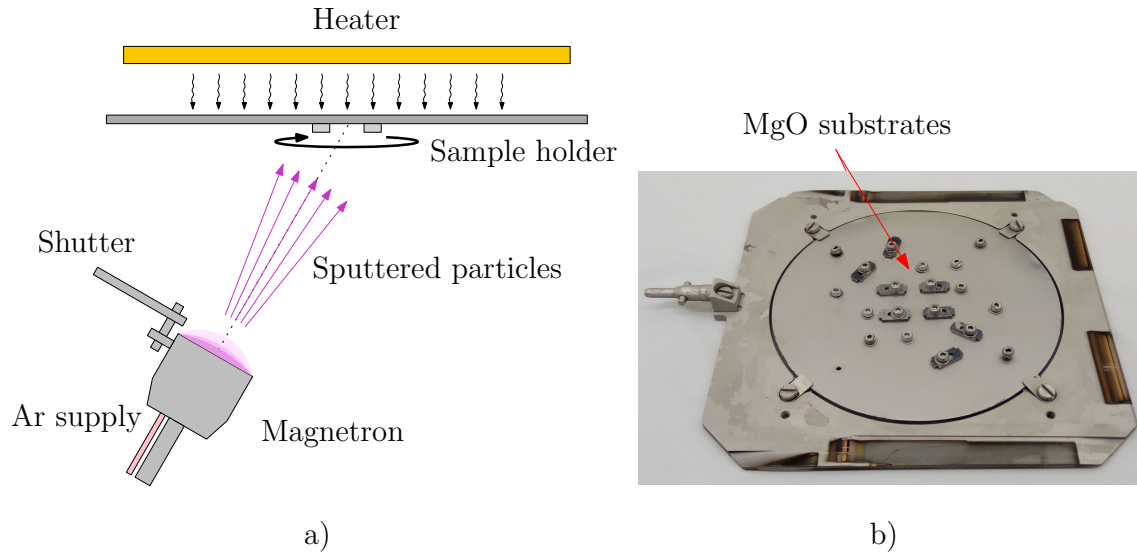


**Fig. 3.2:** a) Scheme of the deposition chamber with a magnetron source with a rotating sample holder. b) Picture of the sample holder with two MgO substrates attached.

As described above, simultaneous deposition from Fe and Rh targets (or crucibles) is a possible way for creating a FeRh layer with the magnetic phase transition [2, 18, 33, 42, 45]. Another way is using an alloy target [22, 29, 30, 42]. In this work, we use a Fe<sub>50</sub>Rh<sub>50</sub> alloy target in Bestec Magnetron Sputtering System in Ceitec Nano Research Infrastructure.

The conditions for FeRh deposition are essential for achieving good crystallographic ordering and presence of the phase transition. It is crucial to maintain the substrate at an optimal elevated temperature during the deposition and then anneal it for a sufficient amount of time. In our work, the heater during deposition was set to 40 % SP power resulting in a temperature of approximately 450 °C to ensure good intermixing of Fe and Rh atoms.

Because of the different vapor pressures of Fe and Rh, the composition of deposited layer depends strongly on the chamber pressure during sputtering [42, 46]. The optimal deposition conditions are summarized in Table 3.1. The resulting deposition rate at these conditions is approximately 0.3 Å/s.

**Tab. 3.1:** Parameters for FeRh deposition.

$T$ (°C)	$Q_{\text{Ar}}$ (sccm)	$p$ (mbar)	$P$ (W)	rotation (rpm)	time (min)
$\approx 450$	50	$2.8 \cdot 10^{-3}$	50	20	variable

The comparison of the phase transition for two slightly different chamber pressures can be found in Fig. 3.3a). The temperature dependence of magnetic moment is shown for FeRh layer deposited with optimal deposition parameters ( $p = 2.8 \cdot 10^{-3}$  mbar) and then annealed for 40 min (red curve in Fig. 3.3) and for a FeRh layer deposited at slightly lower pressure ( $p = 2.7 \cdot 10^{-3}$  mbar) and also annealed for 40 min (dark blue). These two curves were measured in the field of 1 T. The blue curve has a much higher transition temperature than the red curve and the transition is not present below 390 K in 1 T. The light blue curve corresponds to the second sample (deposited at  $2.7 \cdot 10^{-3}$  mbar) measured in the field of 5 T where the transition can be observed because the magnetic field favors the FM phase and reduces the transition temperature.

To obtain the desired crystallographic ordering, the post-annealing process is necessary. The FeRh layers were annealed *in situ* with the heater set point power (SP) set to 70 %. The temperature reached at the sensor was approximately 750 °C. During annealing, the Ar gas supply is closed and the chamber is pumped down to the pressure of around  $10^{-7}$  to  $10^{-8}$  mbar. The duration of annealing process is also very important for setting the FeRh ordered phase. The comparison of samples annealed for 40 and 80 min is shown in Fig. 3.3b). It is visible that for 80 min annealing, the ordering is better established and the phase transition from the AF to FM phase and back is sharper and the thermal hysteresis is narrower.

The sample holder with two  $5 \times 5$  mm<sup>2</sup> MgO substrates is displayed in Fig. 3.2b). The samples are attached by clamps with screws to the circular stainless steel plate.

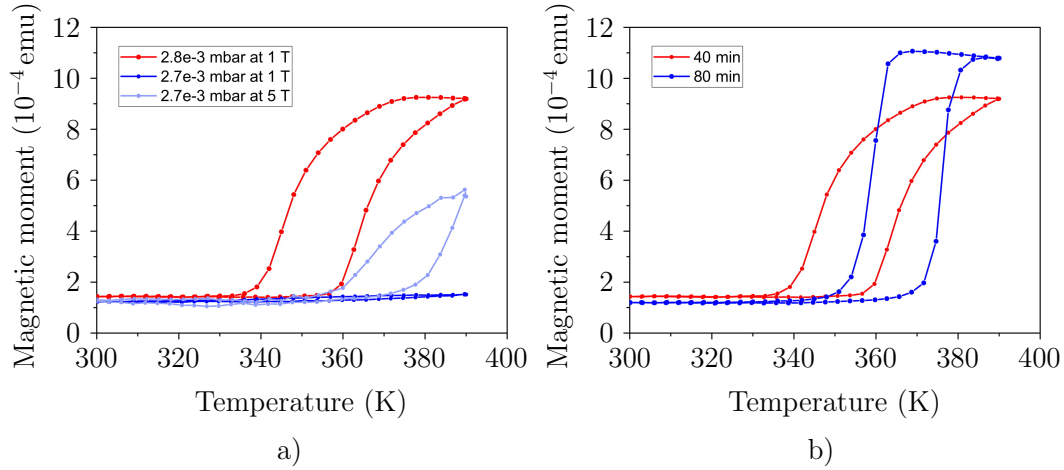


**Fig. 3.3:** The comparison of magnetic moment as a function of temperature for FeRh layers prepared by different protocols. a) red curve shows the transition of the FeRh layer deposited with optimal deposition parameters ( $p = 2.8 \cdot 10^{-3}$  mbar) and then annealed for 40 min and the blue curves correspond to the layer deposited at a slightly lower pressure ( $p = 2.7 \cdot 10^{-3}$  mbar). For the second sample, the phase transition can be only measured at 5 T, which reduces the transition temperature. b) red and blue curves correspond to the sample annealed for 40 min and 80 min, respectively. One can see that for longer annealing the phase is better established and the transition is sharper and narrower.

The sample holder is heated from its back side during the deposition and annealing. However, sometimes the heat transfer from the holder to the sample is not well established and some of the resulting layers were not sufficiently annealed. The result of this is that the samples deposited simultaneously at the same conditions may have different magnetic properties.

### 3.1.2 Substrates

In Chapter 2, it was discussed that the phase transition properties of a FeRh layer depend on the substrate because it induces strain (compressive or tensile in-plane) and by that means modifies the FeRh crystal lattice. The goal of this work is to measure and compare AMR of FeRh layers prepared on different substrates. For this purpose, we use either directly MgO (001) single-crystal substrates to induce compressive strain in the FeRh film or we deposit a thin layer of tungsten (W) on these MgO substrates prior to FeRh deposition to modify the lattice parameter of the substrate.

Deposition of W is an optional step in preparation of FeRh thin films and is also done by magnetron sputtering. Adding the W layer between the MgO substrate and the FeRh layer changes the compressive strain in the FeRh layer to tensile.

Epitaxial BCC W (001) films with a bulk lattice parameter of  $3.165 \text{ \AA}$  grow on

FCC MgO (001) in a  $45^\circ$  rotated position. The lattice parameter of MgO is  $4.212 \text{ \AA}$  which means that half of its face diagonal measures  $2.978 \text{ \AA}$ . This creates a significant lattice mismatch between MgO and W. However, due to strain relaxation, in thick W films, the lattice parameter of the top W layer will be approaching the bulk value. The same phenomenon can be observed for different thicknesses of FeRh films on MgO or W substrates.

The deposition parameters used for sputtering of the W buffer layer on MgO substrate are summarized in Table 3.2. Prior to deposition, the heater inside the chamber was set to 40 % SP power. The corresponding temperature reading on the sensor was approximately  $450^\circ\text{C}$  and got stabilized after 20 minutes. The sample holder was rotating at 20 rpm to distribute the heat and to ensure more homogeneous deposition. The Argon gas flow  $Q_{\text{Ar}}$  was set to 50 sccm and the pressure to  $2.5 \cdot 10^{-3} \text{ mbar}$ . The power used to generate the plasma discharge was 50 W. The deposition rate measured with these settings was  $0.3 \text{ \AA/s}$ .

**Tab. 3.2:** Parameters for W deposition.

$T \text{ } ^\circ\text{C}$	$Q_{\text{Ar}} \text{ (sccm)}$	$p \text{ (mbar)}$	$P \text{ (W)}$	rotation (rpm)	time (min)
$\approx 450$	50	$2.5 \cdot 10^{-3}$	50	20	variable

### 3.1.3 Capping layer

As iron is sensitive to oxidation, it is convenient to cover the FeRh layer with a capping layer to prevent its damage in the air. We usually use Pt capping layer which is deposited on samples after annealing and subsequent cooling. The temperature during the deposition should not be too high so that Pt does not diffuse into the FeRh layer. Deposition parameters are summarized in Table 3.3.

**Tab. 3.3:** Parameters for Pt deposition.

$Q_{\text{Ar}} \text{ (sccm)}$	$p \text{ (mbar)}$	$P \text{ (W)}$	rotation (rpm)	time (min)
50	$2.8 \cdot 10^{-3}$	50	20	30

The whole process of deposition of W\FeRh\Pt layers can be summarized in these steps:

- deposition of a W thin film at an elevated temperature (optional),
- deposition of a FeRh layer at an elevated temperature ( $450^\circ\text{C}$ ),
- *in situ* annealing at high temperature ( $750^\circ\text{C}$ ),
- cooling down the sample,
- deposition of a capping layer (Pt).

## 3.2 Preparation of wires for transport measurement

Top-down approaches for fabrication of nanostructures typically rely on lithography methods using different types of resists. Resist is a chemical compound (usually an organic polymer) sensitive to electrons or ultraviolet (UV) light<sup>1</sup>. In case of a positive resist, the part which is exposed to the electrons or UV light changes its properties and then can be dissolved in a developer. In case of a negative resist, the exposed part is hardened and the developer dissolves everything except for the exposed part.

Examples of positive and negative lithographic processes are illustrated in Fig. 3.4 and 3.5, respectively. In the example of a positive process, the first step is application and exposure of the resist. After development of the resist, a layer of the desired material for nanostructures is deposited. The remaining resist together with the material deposited on top of it is then removed in a solvent. This step is called *lift-off* (Fig. 3.4). In the example of a negative process, the desired material is deposited before coating the sample with a resist. After the exposure and development, the resist serves as a hard mask for ion or wet etching of the material not covered with the resist. In the end the resist is dissolved in a resist remover (Fig. 3.5).

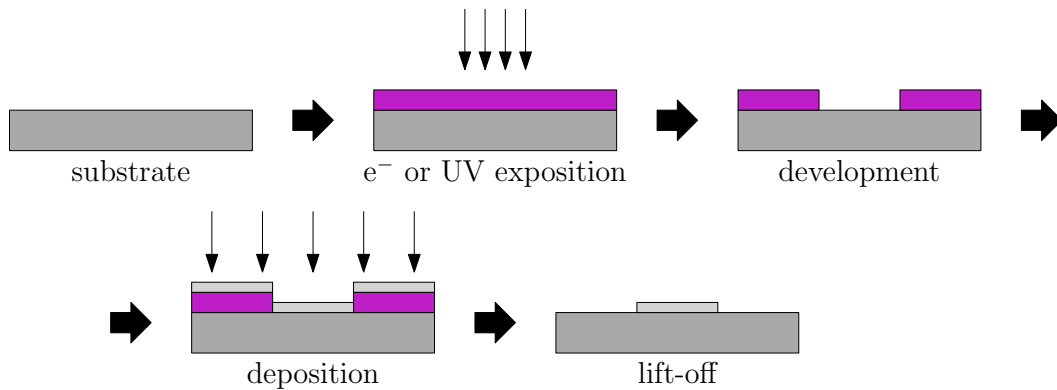


**Fig. 3.4:** Scheme of the lift-off process using a positive resist.

For preparation of FeRh nanostructures the etch process using hard mask was used. The lift-off process cannot be used as the substrate with the resist needs to be heated up to high temperatures during and after deposition of the FeRh film, which would damage the resist.

The final process of FeRh wires preparation uses a combination of the two processes, as the hard mask for etching is patterned from  $\text{SiO}_2$  film using the lift-off process as summarized in Fig. 3.6.

<sup>1</sup>Two types of resists can be distinguished, those which are sensitive to electrons (E-beam resists) and those which are sensitive to UV light (photoresists). Some can be also sensitive to both.



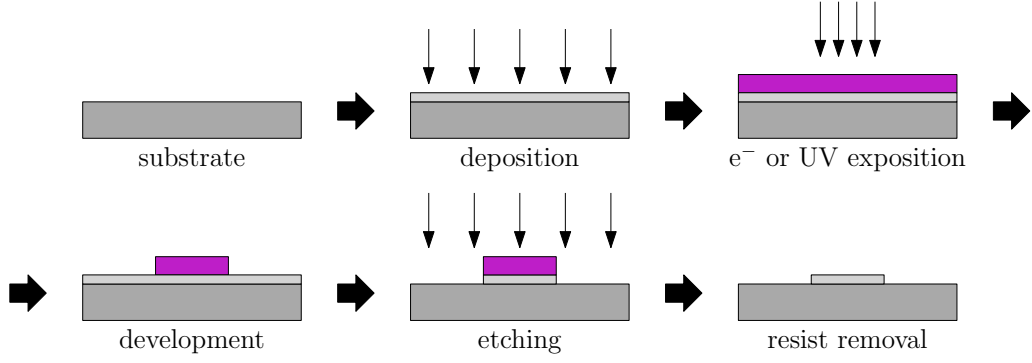


**Fig. 3.5:** Scheme of the etch process using a negative resist.

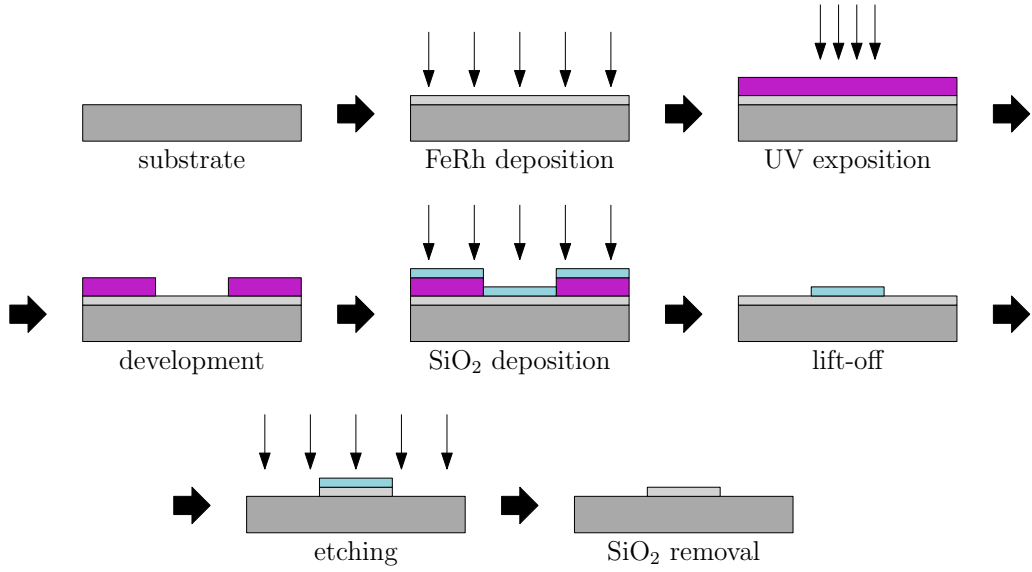


**Fig. 3.6:** Scheme of the full lithographic process used for preparation of FeRh wires.

The lithographic process for preparation of FeRh wires can be then summarized as follows:

- Spincoating of the photoresist (AR-P 5350) at 4000 rpm (accel. 500 rpm/s) for 60 s,
- tempering of the resist at 105°C for 4 min to harden the resist,
- UV exposition through a chromium mask in the Mask Aligner Süss MicroTec MA8 (see Fig. 3.7), a dose of 150 mJ/cm<sup>2</sup> was used,
- resist development in a mixture of AR 300-47 and AR 300-73 in a 3:2 ratio for 80 s, then rinsing with deionized water for 60 s,
- O<sub>2</sub> plasma for 15 s to remove residual resist in the exposed areas,
- SiO<sub>2</sub> deposition: 120-nm-thick SiO<sub>2</sub> layer deposited by electron beam evaporation,
- SiO<sub>2</sub> lift-off in acetone,
- Ar ion etching of the FeRh film (see Section 3.2.1)
- SiO<sub>2</sub> mask removal in buffered oxide etch (BOE) for 2 minutes.

The entire process was carried out in the Ceitec Nano Research Infrastructure.

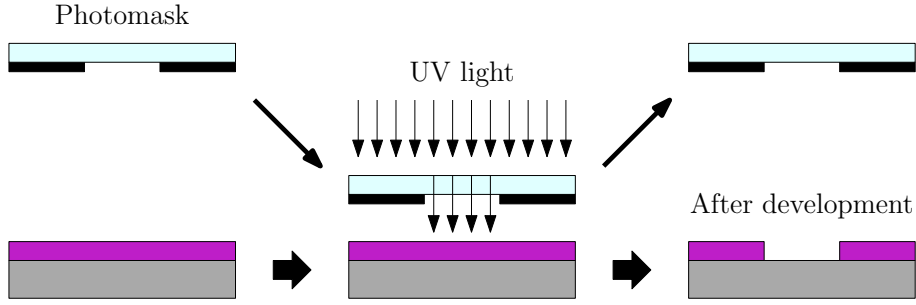


**Fig. 3.7:** Process of UV lithography using a Mask Aligner. A sample with photosensitive resist is put under the mask with a binary pattern. The sample is then pushed towards the mask and is exposed to the UV light. Only the areas not covered with the opaque layer of the mask (for ex. chromium) are exposed on the sample. After development, these areas are washed away.

### 3.2.1 Etching the FeRh film

The FeRh is etched in Ar plasma using the National Instruments PlasmaPro NGP 80 instrument. The gas flow was set to 50 sccm and the pressure to 40 mTorr (approx. 0.053 mbar) and the power of the plasma generator was set to 200 W. With these settings the voltage bias of the generated plasma was about 555 V and the etching rate was found to be approximately 4 nm/min. During the etching procedure, the samples were cooled from the bottom side by a He backing system to prevent excessive heating.

## 4 SAMPLE CHARACTERIZATION

### 4.1 Vibrating sample magnetometry

Vibrating sample magnetometry (VSM) is a method to quantitatively measure the magnetic moment of a sample. The principle of VSM is illustrated by a simple scheme in Fig. 4.1. A magnetic sample is put in a magnetic field which induces magnetization parallel to the applied field in the ferromagnetic part of the sample. The sample is forced into oscillating motion which creates a time-variable stray field. The motion is performed along the axis of a system of detection coils. The alternating magnetic field induces electromotive force in the detection system which is proportional to the magnetic moment of the measured sample. The applied magnetic field also induces diamagnetic response in the sample and sample holder opposing the applied field, which causes reduction of the measured ferromagnetic signal. Because the diamagnetic contribution should not depend on the temperature and exhibits linear dependence on the magnetic field, it can be easily subtracted from the measured data to obtain pure ferromagnetic signal.

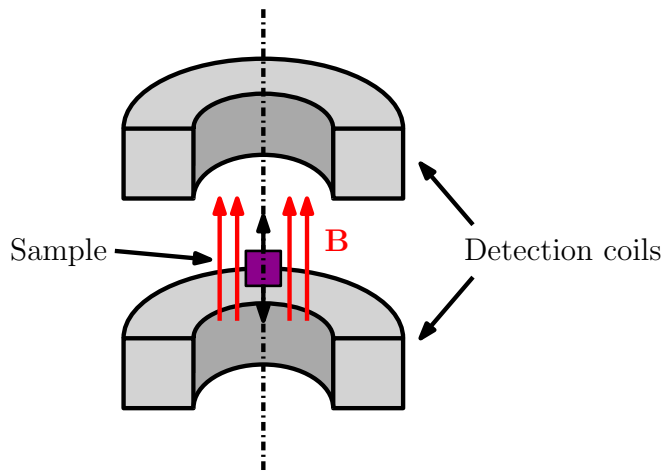


**Fig. 4.1:** Scheme of a Vibrating sample magnetometer. The sample is forced into oscillating motion along the axis of the detection coils. A magnetic field is applied to induce magnetic moment parallel to the axis which induces electromotive force in the detection coils. This response is proportional to the magnetic moment of the measured sample.

In this work, we use VSM to determine the temperature dependence of magnetization of the FeRh layers (before lithography) to detect the phase transition from the AF to FM phase. The net magnetization of an antiferromagnetic ordering is zero, so in VSM we detect only the FM phase of FeRh in the samples. The magnetization curves were measured only for several samples used in the following experiments. The sample with a 40-nm-thick FeRh layer grown directly on an MgO substrate is indicated by the red curve in Fig. 4.2. In the high temperature phase, the magnetic

moment is higher than in the low temperature phase and the phase transition looks complete at 390 K which is a sign that the sample is in the fully FM phase. At low temperatures, the magnetic moment should be zero because the AF phase does not contribute to the total magnetic moment. The non-zero positive magnetic moment at low temperature state indicates a residual FM phase in the fully transformed FeRh layer. This phenomenon was observed and described by F. Pressacco [47] in 2016 in Rh-terminated FeRh layers where they found that the residual ferromagnetic phase is situated in several top atomic layers close to the surface. Anyway, the phase transition of this FeRh layer is sharp and narrow (only 20 K wide) which is a sign of a well-ordered layer.

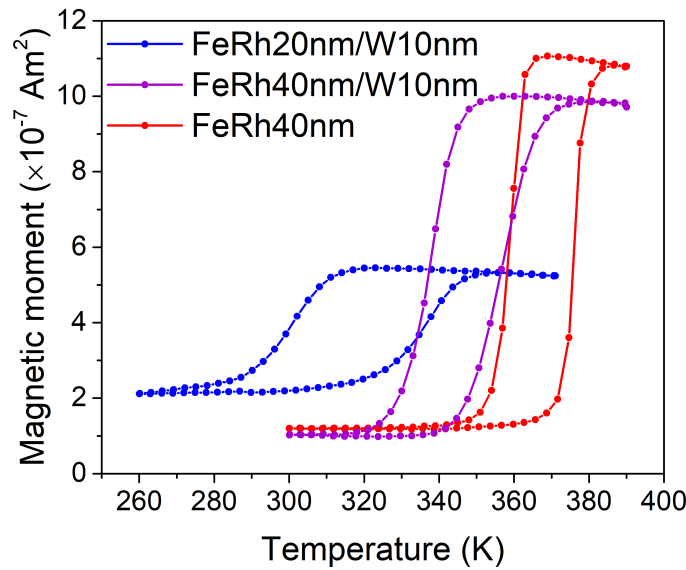


**Fig. 4.2:** Temperature dependence of magnetic moment of three samples measured by VSM. Red curve represents a 40-nm-thick FeRh layer grown directly on a single-crystal MgO substrate, purple curve indicates a 40-nm-thick FeRh layer grown on an MgO substrate with a 10-nm-thick W buffer layer and blue one is a 20-nm-thick FeRh layer on 10-nm-W on MgO.

When comparing the VSM measurements of the 40 nm FeRh layer grown on MgO substrate with a 10-nm-thick W buffer layer (purple curve) with the same FeRh layer grown directly on MgO (red), it is visible, that the phase transition of the layer on W is shifted towards lower temperatures and the phase transition is wider than in the red curve. As mentioned in the theoretical part of this work, tungsten has a bigger lattice parameter than bulk FeRh, therefore it favors the FM phase and reduces the phase transition temperature. This effect is more visible in the thinner FeRh layer (blue) grown on a similar MgO substrate with W buffer layer as the layer is less relaxed than the thicker one. These measurements were carried out at the Institute of Physics of Materials of the Academy of Sciences of the Czech Republic.

## 4.2 Magnetoresistance measurements

The goal of this work was to measure transport properties of wires created from a FeRh thin layer grown on different substrates. The phase transition from the AF to FM phase, which is present in near equiatomic ordered FeRh, can be detected and studied by transport measurements as the resistivities of FeRh AF and FM phases differ significantly, usually by approximately a factor of 2. Therefore during the phase transition, as the FM domains begin to appear, the resistivity of FeRh rapidly decreases. In the temperature regions, where FeRh is in a stable phase, the resistivity increases linearly with temperature as it is expected from a metal.

Besides the study of the phase transition and the resistivity change which accompanies it, this work is concentrated on the measurement of AMR effect in FeRh. To detect the resistivity change due to the AMR, it is necessary to be able to change the direction of magnetic moments in the sample. Or at least, we must be able to orient them in the two extreme positions where magnetic moments are parallel and when they are perpendicular to the electric current.

In this work, two setups were used to measure temperature dependence of resistance of FeRh layers and wires to detect the phase transition and to determine the *AMR* value. These setups are described in the following sections of this chapter alongside the results achieved with them.

### 4.2.1 Magnetoresistance measurement of FeRh nanowires

The Low Temperature Electro-Magnetic Properties Measurement System LakeShore CRX-EM-HF was used to measure resistance of FeRh nanowires across the phase transition. The device is equipped with an electromagnet capable to create an in-plane magnetic field in the sample space up to 500 mT. The system allows to contact the sample with four micro-manipulators to measure its transport properties. These manipulators are illustrated in Fig. 4.3. The manipulators are connected to a setup constituted of a Keithley 6221 current source and a 2182A nanovoltmeter. The setup works in the so-called *Delta mode* which is a method using alternating rectangular wave current to effectively filter out the noise. The device is also equipped with a temperature control system which can set the temperature of the sample in the range from few Kelvin up to approximately 410 K. The temperature control and resistance readout is provided by a LabVIEW program.

The system was tested using a 40-nm-thick FeRh layer grown on an MgO substrate with an aluminum capping layer. It was patterned by electron beam lithography to create nanowires 300-, 500- and 1000-nm-wide. In the one-step lithography the contact pads were patterned with the wire from the FeRh layer to ensure the possibility of a four-probe resistance measurement. VSM measurement of the layer before lithography is depicted in Fig. 4.4a).

The temperature dependences of resistance of 300-, 500- and 1000-nm-wide wires are plotted in Fig. 4.4b)-d). The effect of dimension reduction in two directions

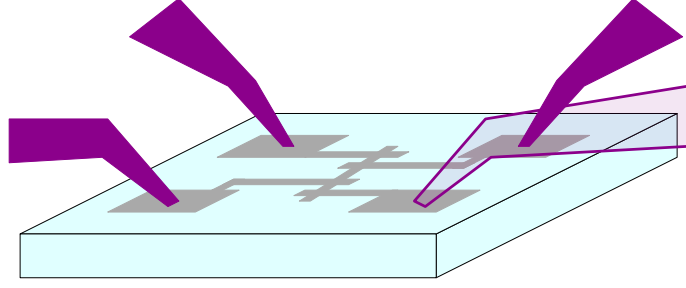


**Fig. 4.3:** Scheme of the FeRh wire with contact pads for four probe measurement. The micro-manipulators (probes) are pushed against the surface of the pads to ensure electric contact. Note that one of the probes in the scheme is transparent only to make the rest of the image visible.

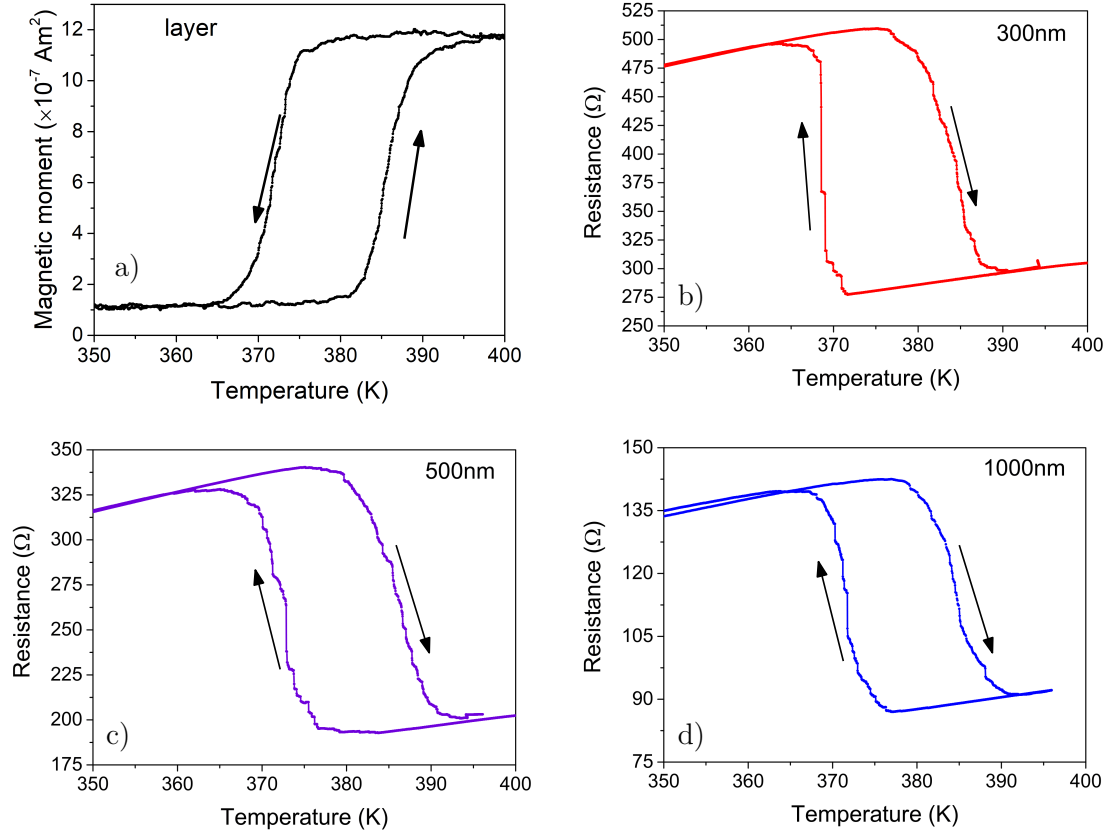


**Fig. 4.4:** a) Magnetic moment as a function of temperature measured by VSM of the 40-nm-thick FeRh layer on MgO used for preparation of 300-, 500- and 1000-nm-wide nanowires. The temperature dependence of resistance of the corresponding b) 300-nm, c) 500-nm and d) 1000-nm-wide wires.

(thin layer and narrow wire) described in literature [39], is clearly visible in our measurements. During the heating cycle, the resistance changes continuously but during the cooling cycle, the resistance changes abruptly in several steps (see also

Section 2.3). The effect is more pronounced in the narrower wires. A little shift of the phase transition towards lower temperature for narrower wires is also visible in Fig. 4.4. This is caused by the fact that a narrower wire gets more easily relaxed on the substrate than the wider ones and therefore in the FeRh wire, the lattice parameter and the phase transition temperature get closer to its bulk values.

### 4.2.2 AMR measurement of FeRh stripes

The AMR measurements require the possibility to rotate the sample in a magnetic field without the necessity to reconnect the wires for transport measurement. A new setup was assembled by employing already existing devices and designing a new sample holder. The assembly is illustrated in Fig. 4.5. The assembly allows the application of a magnetic field up to 400 mT in-plane of the sample by an electromagnet powered by the Kepco BOP 20-10M current source. An integrated motorized continuous rotation stage Thorlabs CR1/M-27 provides the rotation movement of the sample holder controlled by computer.

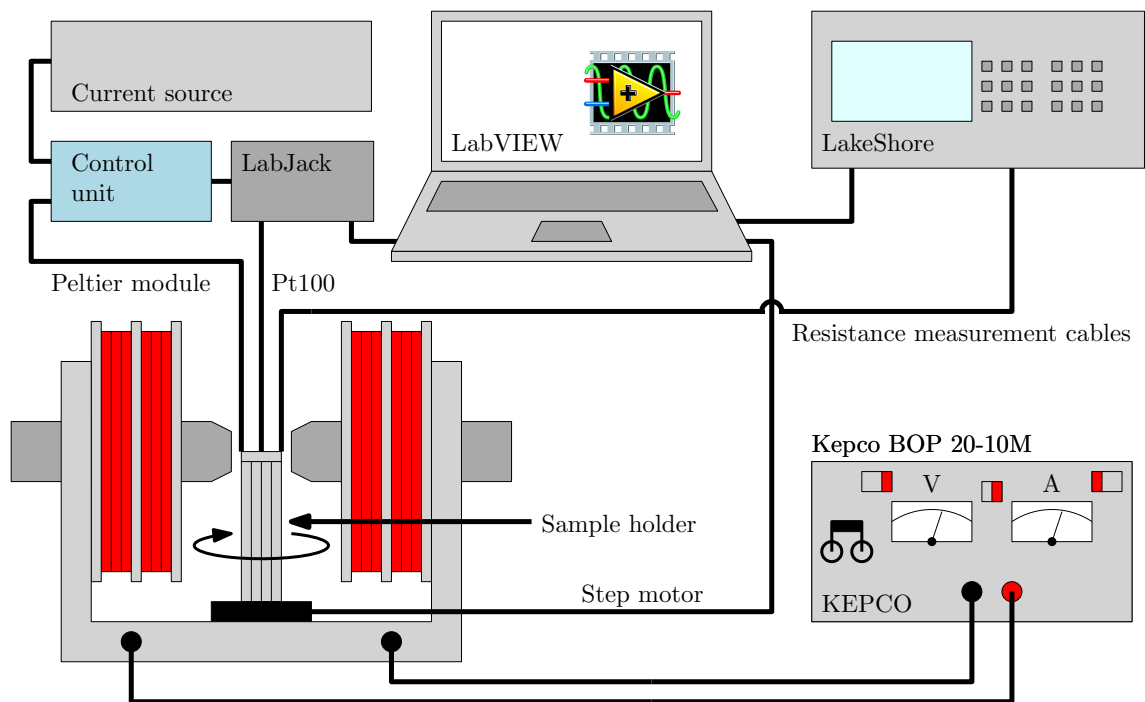


**Fig. 4.5:** Scheme of the setup for measurements of AMR by rotating the sample in a magnetic field. In this setup, it is possible to control magnetic field, temperature at the sample and measure the resistance with the four-probe method.

The new sample holder enabling the temperature control and transport measurements with the rotation stage is shown in Fig. 4.6. The main part of the sample holder is a duralumin body composed of two pieces. The bigger part is attached with threads to the rotation stage and to the smaller duralumin part. A double stage Peltier module is glued with silver paint to the top of this assembly and covered with

a PCB<sup>1</sup> which is screwed to the duralumin body. The PCB was designed with two rectangular windows located above the top part of the Peltier stage. In the smaller window a Pt100 temperature sensor is glued with silver paint to the Peltier stage to ensure direct and precise temperature readout and the bigger window is dedicated for the measured  $5 \times 5 \text{ mm}^2$  sample. There are six printed connections for transport measurement located around the sample window.

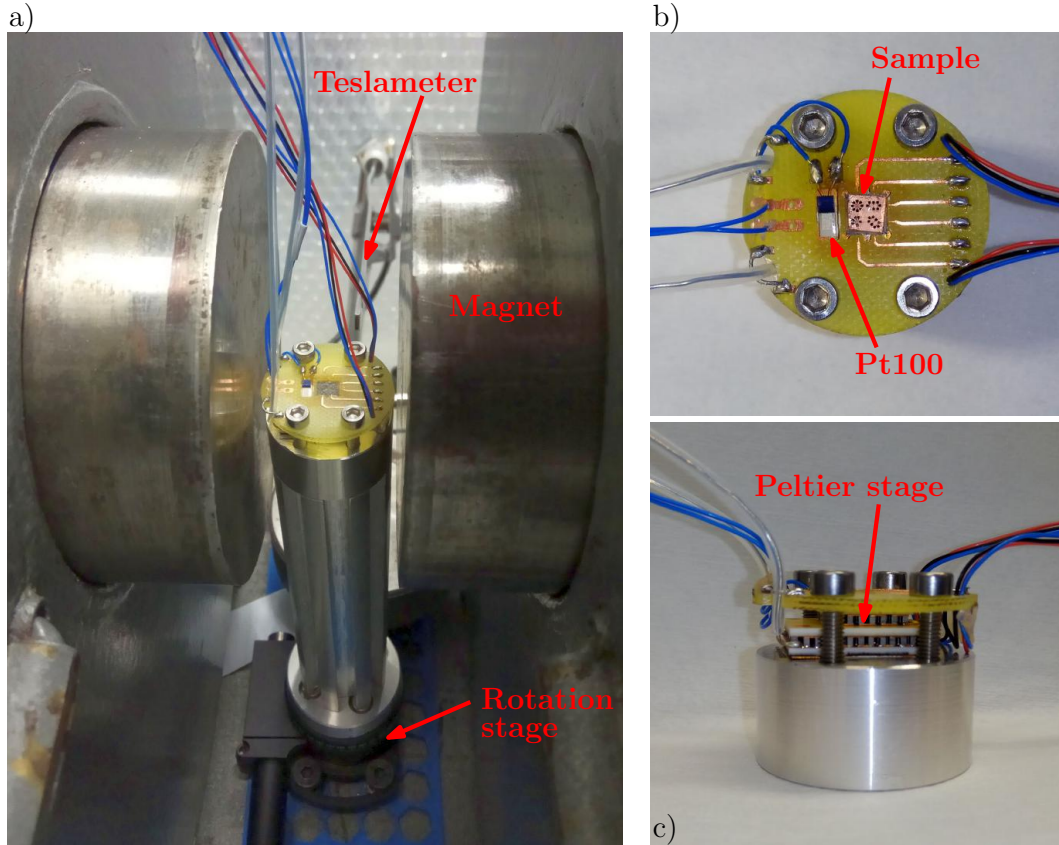


**Fig. 4.6:** Images of the sample holder for AMR measurements. a) The duralumin sample holder placed between poles of the electromagnet with the Teslameter in the background for magnetic field measurement. The rotation stage is visible in the bottom part of the image. b) and c) are top and side views of the upper part of the sample holder. Placement of the Pt100 temperature sensor, sample and Peltier stage is shown.

The temperature is controlled by a LabVIEW program with a PID regulator. The program communicates with a DAQ LabJack U3 HV which assures Pt100 resistance reading and therefore it provides the information about the temperature. The LabJack is also connected to a control unit which sends electric current into the Peltier stage according to the PID regulator signal. The duralumin sample holder

---

<sup>1</sup>Printed circuit board



body serves also as a heat sink for thermal dissipation from the bottom part of the Peltier module.

Concerning the transport measurement, the sample can be wire-bonded to six separated printed connections which can be arbitrarily connected to two current and two voltage pins going from the LakeShore Cryotronics AC Resistance Bridge. This device allows to measure the resistance with four-probe method using an alternating current. The LabVIEW program also provides the communication with this device and readout of the resistance measurement.

In this setup, the angle describes the orientation of the magnetic field and thus we assume magnetization is aligned with it. The angular dependence of resistance of FeRh stripes is measured at different temperatures. For determination of the *AMR*, a Matlab script is used that fits the measured angular dependence of resistance with the function

$$R(\theta) = a + b\theta + c\theta^2 + d\cos(\theta - \beta). \quad (4.1)$$

This function is modified (1.17) where terms with  $\theta$  and  $\theta^2$  are added to compensate the resistance drift due to the temperature instability during one cycle of the measurement. The constants  $a$  and  $d$  coming from the fit represent the resistance  $R_{\perp}$  when the magnetization is perpendicular to the electric current and the resistance difference  $R_{\parallel} - R_{\perp}$ , respectively. The value of *AMR* can then be extracted as  $AMR = d/a$  (1.18).

Illustration of a measured angular dependence of resistance with AMR and temperature drift is depicted in Fig. 4.7a). This dependence can also be put in a polar graph which provides better visualization of the AMR effect (Fig. 4.7b)).

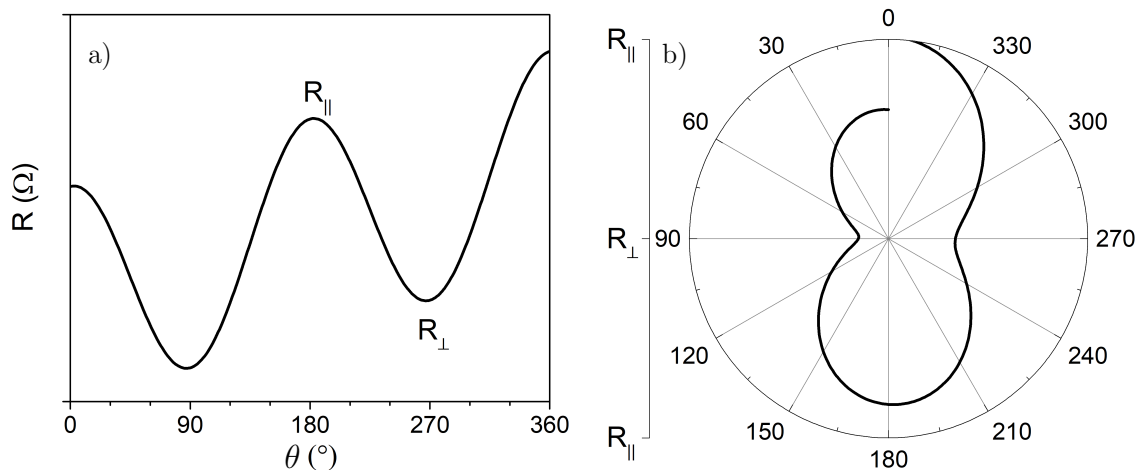


**Fig. 4.7:** Example of measured angular dependence of resistance with a significant thermal drift a) in a regular plot and b) in a polar plot.

### Calculation of FeRh resistance in FeRh/W stripes

The stripes patterned from the samples of FeRh on MgO substrate with a W buffer layer constitute of two conductive layers. We do not take into account the Pt capping layer which is also present in the measured stripes. The W layer in our samples is 10 nm thick which is comparable to the thickness of the FeRh layer. There is no gap between the two layers and therefore when measuring the resistance of the stripes, we are measuring the resistance of the overall system. Because we want to study the relative resistance change of FeRh (AMR), we use a simple method to get rid of the W contribution to the total resistance.

We used a 10-nm-thick W layer on an MgO substrate prepared by the same process as for the buffer layer in order to prepare a reference stripe structure. We measured the temperature dependence of the resistance to determine the W resistivity and the temperature coefficient  $\alpha$ . In the range of temperatures we use, the resistivity can be expressed as

$$\rho(T) = \rho_{300} + \alpha(T - 300) \quad (4.2)$$

where  $\rho_{300}$  is resistivity at 300 K and  $T$  is absolute temperature. The determined values are given in Table 4.1.

**Tab. 4.1:** The resistivity  $\rho_{300}$  at 300 K and the temperature coefficient  $\alpha$  of the W layer.

$\rho_{300} \text{ (}\Omega\text{m)}$	$\alpha \text{ (}\Omega\text{m/K)}$
$4.3 \cdot 10^{-7}$	$2.7 \cdot 10^{-10}$

The formula for two parallel resistors

$$\frac{1}{R} = \frac{1}{R_1} + \frac{1}{R_2} \quad (4.3)$$

is used to determine the FeRh contribution to resistance  $R_1$  out of the resistance of the system  $R$  and the resistance  $R_2$  of the W contribution calculated from its resistivity and dimensions of the measured stripe<sup>2</sup>. All measured data in samples with W buffer layer were processed in Matlab to calculate the FeRh contribution to the resistance.

---

<sup>2</sup>It is calculated from the formula  $R = \rho \cdot l / (w \cdot t)$  where  $l$ ,  $w$  and  $t$  are length and width of the stripe and  $t$  is the thickness of the tungsten layer, respectively.

## 5 AMR IN FERH WIRES

The main focus of this work is on the study of AMR in FeRh wires. In this chapter, we pursue the description and understanding of the phenomena occurring in FeRh lithographically prepared wires.

### 5.1 AMR in FeRh nanowires

The Lakeshore system described in Section 4.2.1 allows to apply magnetic field up to 500 mT and contact the sample using micro-manipulators for four-probe measurement of electric resistance. This setup does not allow to rotate the sample without disconnecting the micro-manipulators from the sample. Despite the the four-probe measurement, the process of disconnecting and reattaching probes brings a significant resistance change (0.01-0.1  $\Omega$ ), which is comparable to the expected *AMR* in FeRh. Therefore it is impossible to measure the *AMR* in the AF phase of FeRh in this setup by comparing the resistance values after field cooling with magnetic field applied parallel and perpendicular to the current.

Nevertheless, the *AMR* of the FeRh FM phase at high temperature can be measured by benefiting from the shape anisotropy present in the nanowires. The demagnetizing field caused by the elongated shape of the wire structure forces the magnetization to align along the long axis of the wire, i.e. parallel to the electric current. By applying magnetic field perpendicular<sup>1</sup> to the nanowire, i.e. along the hard axis, the magnetization is tilted in the direction of the external field.

The magnetic field dependence of resistance with in-plane magnetic field applied perpendicular to the nanowire was measured in three wires with different widths (300 nm, 500 nm and 1000 nm) prepared from a 40 nm thick FeRh layer on an MgO single-crystal substrate. The measurement was done at 400 K, where the sample should be fully ferromagnetic. The results with the resistance normalized to the zero-field value, which is one of the ways to define *AMR*, for the three wires is displayed in Figs. 5.1a)-c). The graphs show that with increasing magnetic field the resistance decreases as the magnetization is rotated perpendicular to the nanowire. The sharpness of the curve decreases with increasing the width of the wire suggesting that the saturation field is smaller for wider wires. This effect can be explained by the increasing demagnetizing field creating a stronger shape anisotropy along the narrower wires. Therefore, higher magnetic field is necessary to overcome the shape anisotropy in narrower wires.

At high magnetic fields, the resistance seems to show a linear decrease. This effect is caused by suppressing thermal excitation of magnons by the action of magnetic field. The suppression is more effective for a higher intensity of the field. For ordinary ferromagnetic materials, the sample can be cooled down to low temperatures to

---

<sup>1</sup>In this chapter, the perpendicular orientation stands for the transverse direction of the magnetic field with respect to the wire/stripe in plane of the sample.

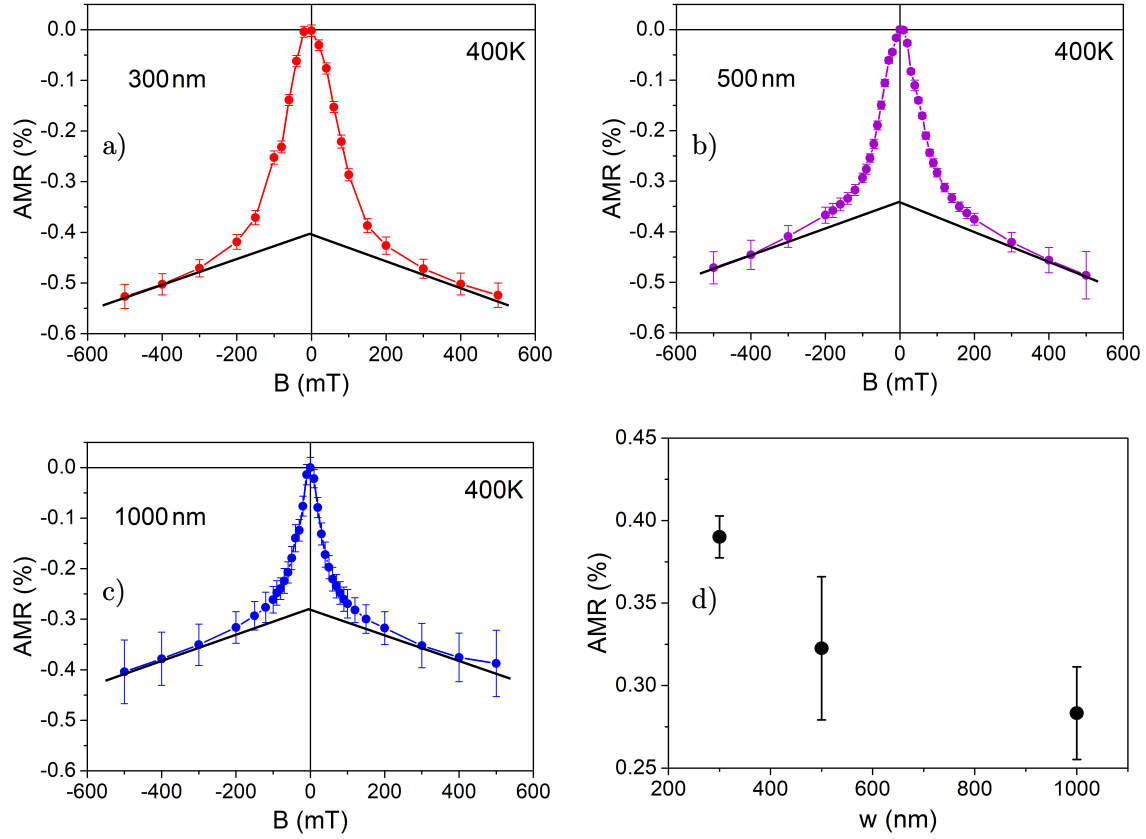


**Fig. 5.1:** Measurement of AMR in nanowires patterned in 40 nm thick FeRh film. The magnetic field dependence of the resistance normalized to its zero-field value (AMR) for a) 300 nm, b) 500 nm and c) 1000 nm wide wires. Black lines show the magnon damping effect and the zero field intersection. d) The *AMR* amplitude taken from the intersection of the fitted linear line at higher field with the zero-field axis for different widths of the wires.

reduce the effect of magnon oscillations. This method is not applicable for FeRh as it loses its FM properties at low temperatures and transforms into AF. To compare the *AMR* amplitude for different wires, we eliminate this effect by fitting the linear part of the curves and compare the AMR at the intersection with zero field axis. These values are arranged in Table 5.1 and plotted in Fig. 5.1d). According to these results, the *AMR* amplitude increases with decreasing the width of the wire. In order to explain this behavior, micromagnetic simulations were executed in OOMMF<sup>2</sup>.

**Tab. 5.1:** The comparison of *AMR* values for different widths of the wires after compensating for the effect of magnon damping.

width (nm)	300	500	1000
<i>AMR</i> (%)	-0.40	-0.34	-0.28

<sup>2</sup>Object Oriented MicroMagnetic Framework

For simulation of the dependence on the nanowire width, we simplify its shape to a rectangular block with a thickness of 40 nm and the ratio of the two other sides is used as 1:5 to express the elongated shape of the wires in the  $y$  direction. The rest of the parameters used in the calculations are summarized in Table 5.2.

**Tab. 5.2:** Calculation parameters for micromagnetic simulations of FeRh nanowires.

cellsize (nm <sup>3</sup> )	Exchange stiffness $A$ (J/m)	Magnetization $M_S$ (A/m)
$2 \times 2 \times 40$	$1.0 \cdot 10^{-11}$	$1.3 \cdot 10^6$

We use the process of energy minimization to determine the magnetization state of the FeRh block in changing magnetic field. The magnetization layout for every magnetic field is loaded into a Matlab program where the resistance is calculated for every cell from the following relation:

$$R_i = R_{\perp} + AMR \cdot R_{\perp} \cdot (M_{iy}/M_S)^2, \quad (5.1)$$

where  $R_{\perp}$  is the resistance of a cell when magnetization  $M_i$  is perpendicular to the current,  $AMR$  is defined by (1.18) (for the calculation it was set to 1 %) and  $M_{iy}/M_S$  expresses the cosine of the angle between the magnetization and current which flows in the  $y$  direction. The total resistance of the system is calculated from the relations for resistors connected in a parallel and serial configuration, but only in the middle part of the wire (highlighted in Fig. 5.2a)). The exclusion of the outer regions serves to suppress the effect of perturbation of magnetization at the ends of the wire.

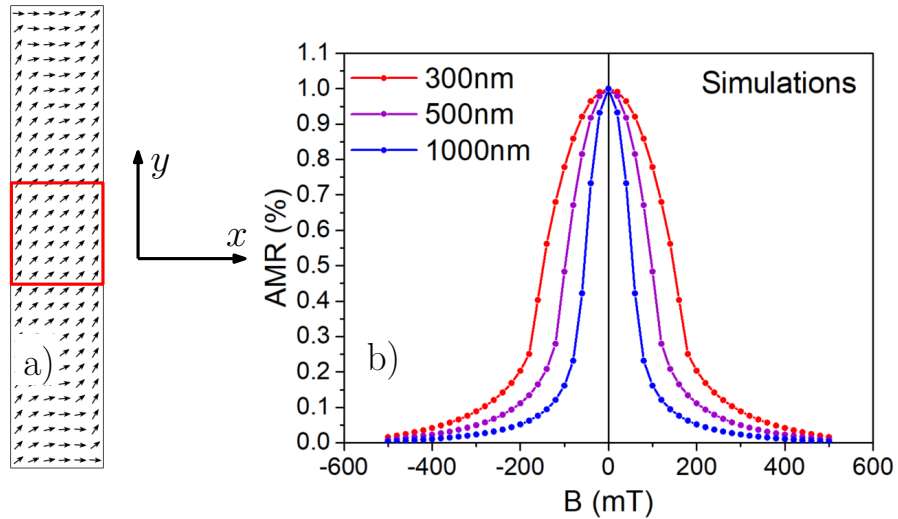


**Fig. 5.2:** a) Example of a magnetization map for a 300-nm-wide and 1500-nm-long wire. The red rectangle illustrates the region where the resistance is calculated from the magnetization orientation. b) Simulated dependence of  $AMR$  on magnetic field for different widths of the wires.

The results of these calculations (plotted in Fig. 5.2b)) show that the magnetic field dependence of the *AMR* is wider for narrower wires. The simulated curves are also wider than the measured ones and this can be explained by the effect of the roughness of surface in real wires which weakens the shape anisotropy. In the simulations, we do not take into account the effect of magnon excitation and therefore we do not observe a decrease of resistance with increasing intensity of the magnetic field.

The micromagnetic simulations were carried out in order to explain the decrease in the *AMR* amplitude with increasing width of the wire. But it is apparent, that in all three cases, the magnetization in higher applied fields (500 mT) is tilted almost perpendicular to the current in the whole region of interest and thus gives lowest resistance possible for the wire. Therefore these magnetic simulations cannot explain the *AMR* amplitude change. Even though the simulations show that in zero field the magnetization aligns perfectly along the wire, it does not take into account thermal excitations or the roughness of the structure which could cause a disorder in the magnetization. The demagnetizing field exerting on magnetization is smaller in wider nanowires and thus in a real system, the magnetization is better aligned along the narrower nanowire in zero magnetic field. This effect could be the reason of *AMR* decrease in wider nanowires.

As this LakeShore system does not allow sample rotation to quantitatively evaluate the *AMR* in FeRh nanowires, a different setup was designed for *AMR* measurements. We also decided to exchange the nanowires for larger structures (few microns wide) as the shape anisotropy is quite big for these nanowires while the magnetic field necessary to overcome the anisotropy field is close to the maximum we can apply. In wider wires, the shape anisotropy is not that pronounced and thus the magnetic field necessary to orient the magnetization in the perpendicular direction is significantly smaller.

## 5.2 *AMR* in FeRh stripes

The way to measure *AMR* of the FeRh FM phase with the new setup is to apply static magnetic field and rotate the sample in it. As the sample changes its orientation the magnetic field is applied in different directions with respect to the wire. The magnetization of the FM phase aligns with the field and thus when rotating the sample, the relative angle between the magnetization and electric current changes. The resistance dependence on angle should fit the cosine square function (1.18) and the resistance maximum should be aligned with the direction of the current.

In the previous chapter, a new setup for this type of measurement was presented along with the protocol for processing the measured data. Several samples with different thicknesses of the FeRh layer grown directly on an MgO single-crystal substrate or on an MgO substrate with a 10-nm-thick W buffer layer were used for preparation of microstructures for magnetoresistance measurements. The graphs

of temperature dependent resistance showing the phase transition of the fabricated samples are plotted in Fig. 5.3 and Fig. 5.4. The shape of the phase transition varies for different samples and in thinner FeRh layers, the transition temperature is smaller. The shift of the phase transition to lower temperatures caused by the W buffer layer is also observed.

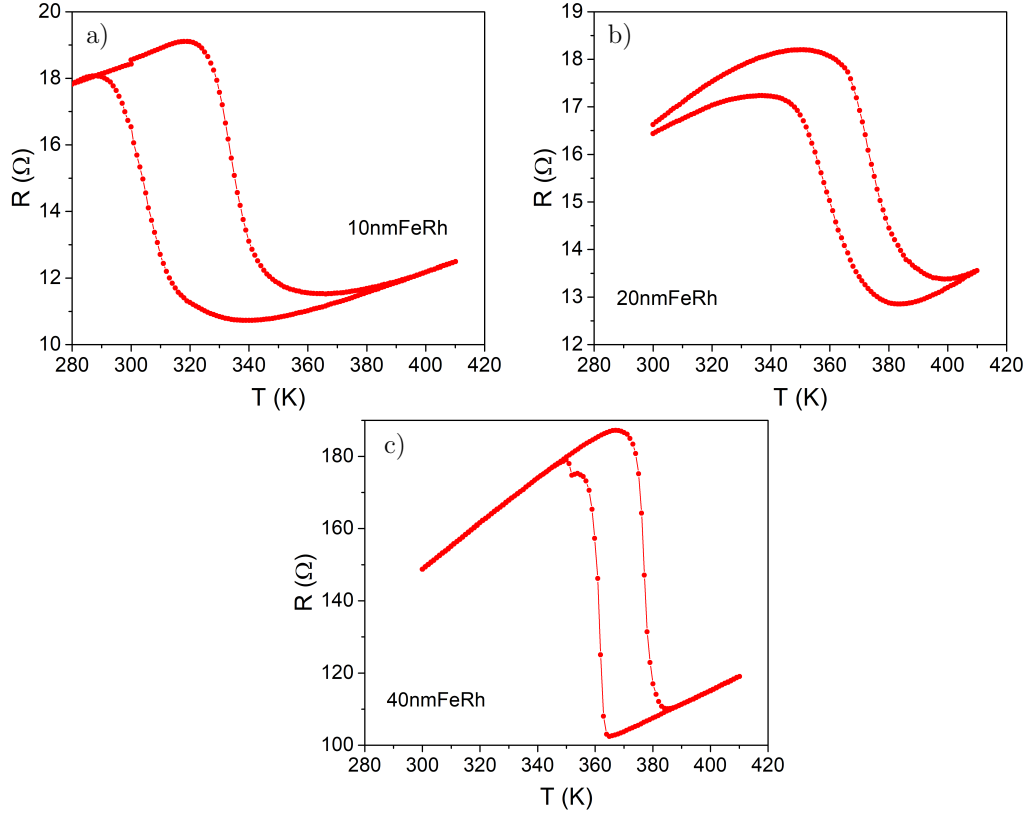


**Fig. 5.3:** Temperature-dependent resistance of a) 10-nm-thick and b) 20-nm-thick FeRh layer and c) 40-nm-thick and 7- $\mu$ m-wide FeRh stripe on an MgO substrate.

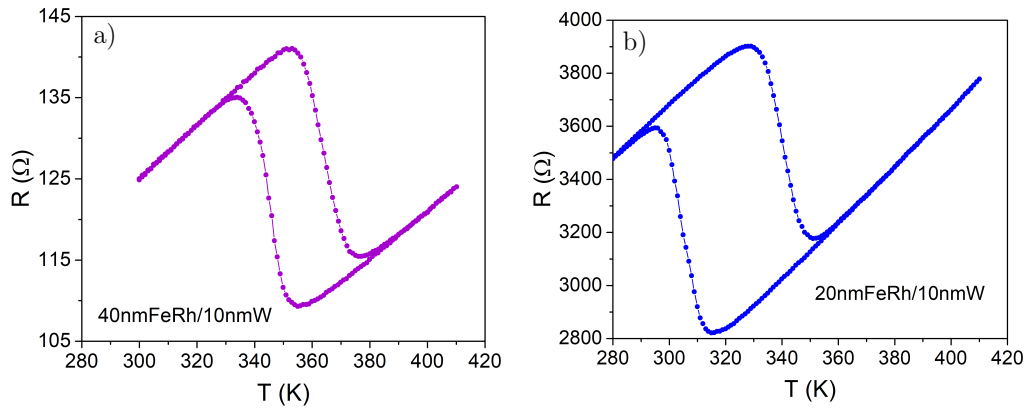


**Fig. 5.4:** The temperature dependence of resistance of a FeRh stripe on W-covered MgO substrate with a thickness a) 40 nm and b) 20 nm.

As was described in Chapter 4, we determine *AMR* of the FM phase of FeRh by rotating the sample in magnetic field and thus measuring the angular dependence of resistance. The resistance should be maximal for the orientation when magnetization is parallel to the electric current and minimal when they are perpendicular. We measure this angular dependence at a high temperature (410 K) where FeRh is fully in the FM phase and at a low temperature (300 K or eventually 280 K) where FeRh is almost fully transformed into the AF phase with only a small portion of the residual FM phase.

The dependence of resistance on the field cooling direction was performed to determine the *AMR* of the FeRh AF phase. The magnetic field orientation with respect to the stripes was set parallel and perpendicular during the cooling of the sample. These two types of cooling procedures are labeled as  $\parallel FC$  and  $\perp FC$  for the magnetic field of 400 mT oriented parallel and perpendicular to the measured stripe, respectively. After the field cooling the spin axis of the AF phase should be oriented perpendicular to the direction of the applied magnetic field.

### 5.2.1 Angular dependence of *AMR* in FeRh stripes

The 40-nm-thick FeRh layer grown epitaxially on a single-crystal MgO substrate as illustrated in Fig. 5.5a) was patterned using UV lithography into microstructures for transport measurements. The FeRh crystal grows on MgO rotated by  $45^\circ$ , i.e. the main crystal direction [100] of FeRh is along MgO [110] direction. Fig. 5.5b) illustrates the shape of this microstructure. The patterned structure constitutes of three stripe segments oriented along different crystallographic directions connected to 6 pads for microbonding. Microstructures with three different widths of stripes (5  $\mu\text{m}$ , 7  $\mu\text{m}$  and 12  $\mu\text{m}$ ) were prepared on one sample. The polar plots of measurements on the 7- $\mu\text{m}$ -wide stripe at 410 K and 300 K are presented in the following figures.

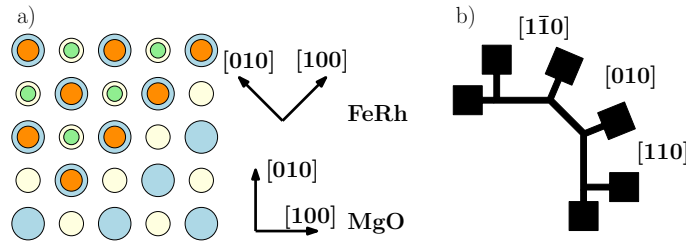


**Fig. 5.5:** a) Scheme of FeRh growth on an MgO single crystal with notion of the crystal directions in MgO and FeRh. b) The pattern of the stripe structure for four-probe resistance measurement of segments along different crystallographic directions.

In the first segment of 7- $\mu\text{m}$ -wide stripe, the electric current flows in the direction  $[1\bar{1}0]$  and the angular dependence of resistance measured with different magnitude of applied magnetic field at the fully FM phase (410 K) is plotted in Fig. 5.6a). The



resulting polar plots show, that the maximum of resistance lies along the direction of electric current (90 and 270°) and the minimum in the direction perpendicular to it (0 and 180°). The curves for different magnetic field magnitudes do not seem to change with the exception of 10 mT, where the field is too weak to saturate the magnetization perpendicular to the stripe and therefore the resistance does not reach its minimal value.

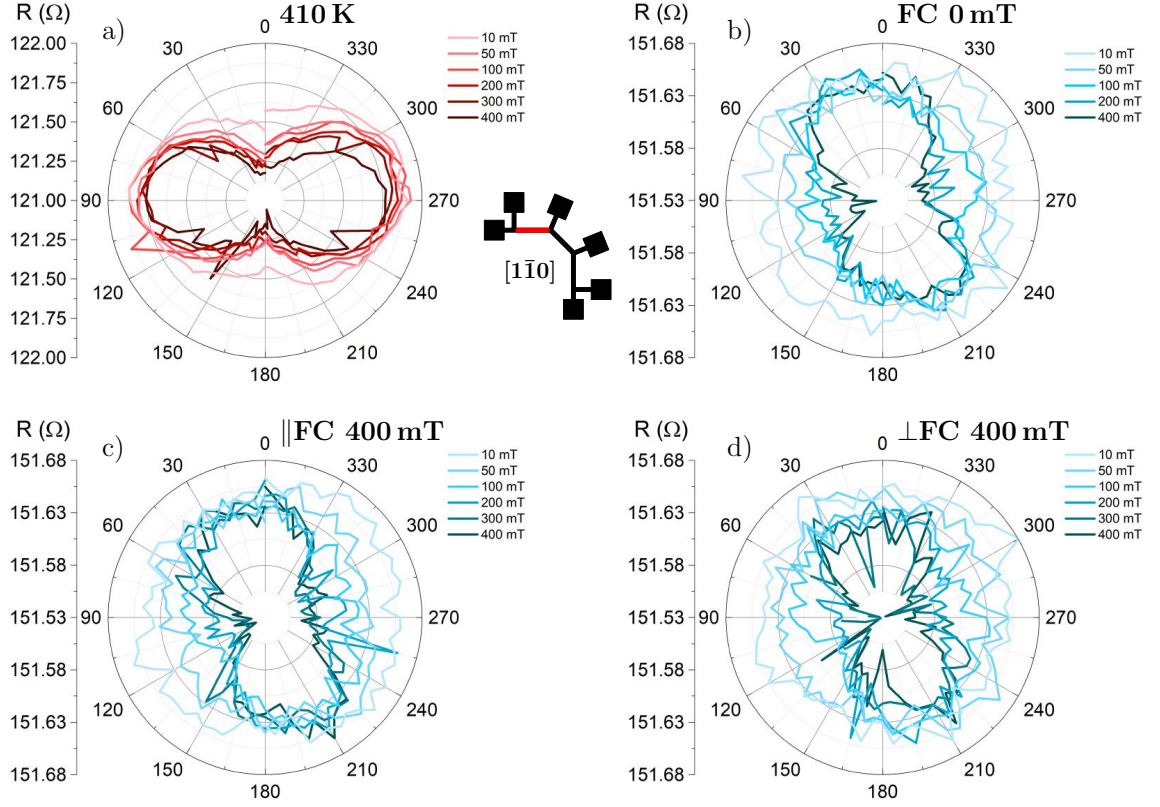


**Fig. 5.6:** Polar plot of angular dependence of resistance on the magnetization direction of the 40-nm-thick FeRh stripe on an MgO substrate oriented along  $[1\bar{1}0]$  crystal direction measured with different magnitudes of magnetic field a) at 410 K, at 300 K after field cooling in b) no magnetic field, in c) 400 mT  $\parallel$ FC and d)  $\perp$ FC.

The polar graphs for the  $[1\bar{1}0]$  segment in the AF phase (300 K), where only a small portion of residual FM phase should be present, are plotted in Fig. 5.6b), c) and d) corresponding respectively to field cooling in zero magnetic field, and 400-mT  $\parallel$ FC and  $\perp$ FC to the stripe. The measurements were again done at various magnitudes of magnetic field. The value of resistance and the shape and orientation of the polar graph relating to these three cooling procedures do not change thus the effect of the AF phase orientation on the FM AMR was not proved. When comparing the polar graphs in the low temperature phase with the high temperature phase, an unexpected rotation of approximately  $75^\circ$  is observed. The shape of the angular dependence changes with the decreasing magnetic field and the magnetization seems to stay in the high resistance state because for lower magnitude of field, the resistance

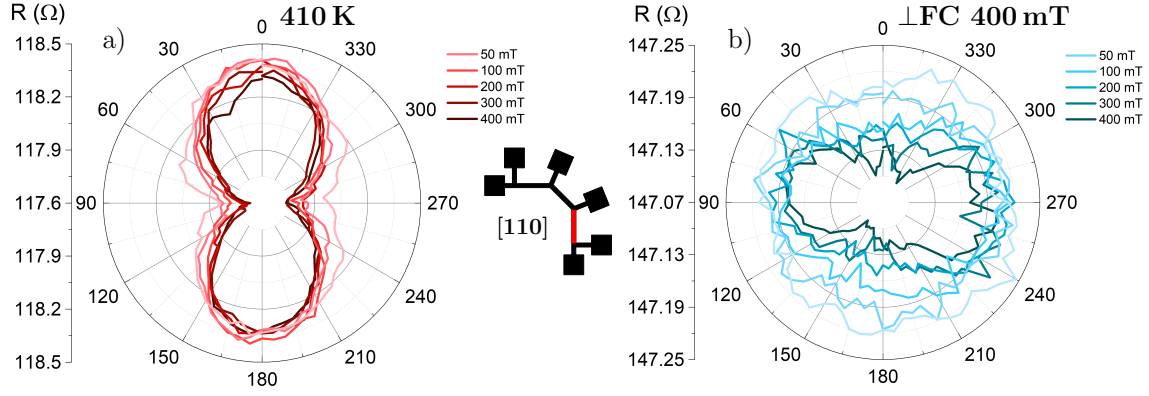


**Fig. 5.7:** Polar plot of angular dependence of resistance on the magnetization direction of the 40-nm-thick FeRh stripe on an MgO substrate oriented along  $[110]$  crystal direction measured with different magnitudes of magnetic field a) at 410 K, at b) 300 K after field cooling in 400 mT  $\perp$ FC.

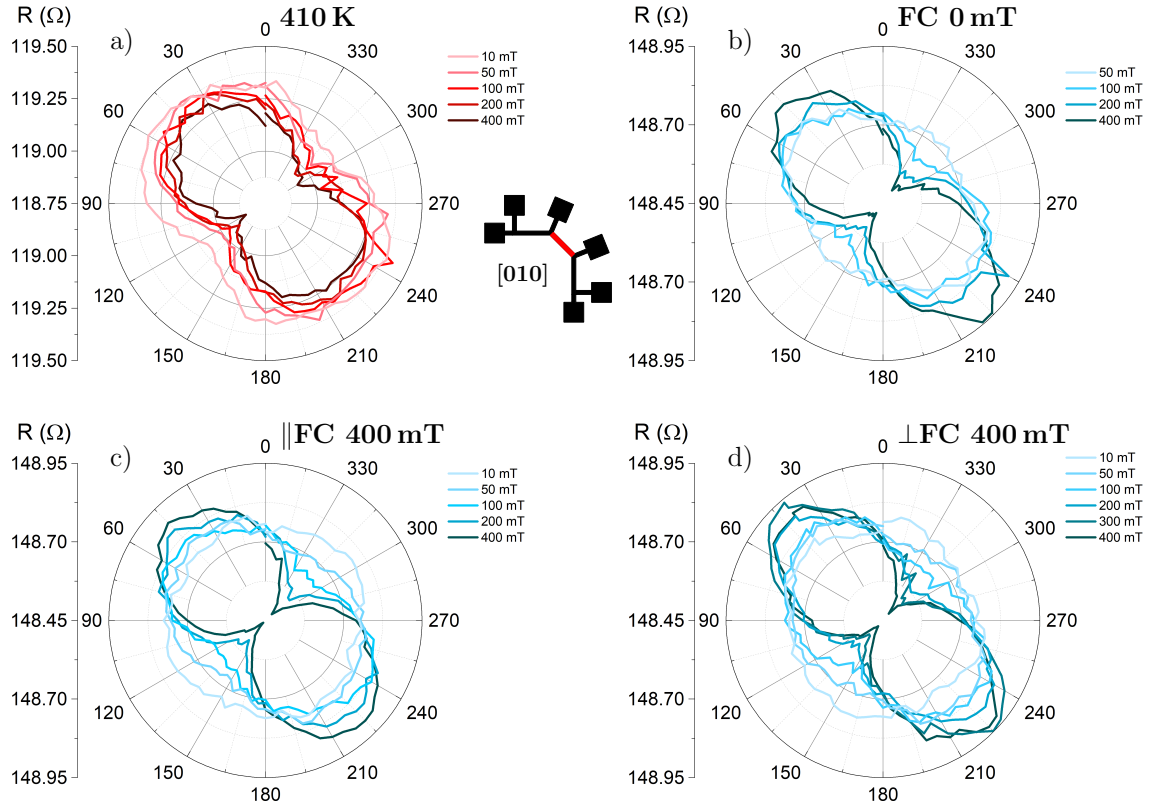


**Fig. 5.8:** Polar plot of angular dependence of resistance on the magnetization direction of the 40-nm-thick FeRh stripe on an MgO substrate oriented along  $[010]$  crystal direction measured with multiple magnitudes of magnetic field a) at 410 K, at 300 K after field cooling in b) no magnetic field, in c) 400 mT  $\parallel$ FC and d)  $\perp$ FC.

does not reach the lowest measured value and the amplitude of  $AMR$  decreases. However, application of a high magnetic field along the stripe, which reinforces the orientation of the magnetization along the stripe and current direction, i.e. along the conventional high resistance direction, leads to a significant decrease of resistance.

The same set of measurements was performed for the other two segments where current flows along  $[010]$  and  $[110]$  crystallographic directions. For the  $[110]$  segment, the results are similar to the segment  $[110]$  (Fig. 5.7a) and b)), only they are rotated by  $90^\circ$  so that in the high temperature phase (410 K) the maximum resistance value is aligned along the stripe. Concerning the three different cooling protocols the data again show no significant difference.

In the diagonal segment, where current flows in the  $[010]$  direction, the shape of the polar graphs in the high temperature state (410 K) is comparable to the other two segments (Fig. 5.8a)). The maximum resistance lies in the direction  $45^\circ/225^\circ$  which is in agreement with the orientation of the stripe. However, in the low temperature phase (300 K), the position of the maximum is at the same angle as in the case of the high temperature phase. Again the three cooling procedures give the same result as shown in Fig. 5.8b)-d). The low temperature phase measurements demonstrate that with lower magnetic field applied during the measurement, the resistance does not reach the maximum or the minimum value and therefore the magnetization tends to stay in the arrangement with a medium resistance value.

The same set of measurements was also performed for the stripe width of  $5\ \mu\text{m}$  and  $12\ \mu\text{m}$  and it shows the same behavior as described above. All these measurements were processed by Matlab in the way described in Chapter 4 and the value of  $AMR$  was determined. The  $AMR$  values for the three stripe segments of different width are plotted in Fig. 5.9a) where red points are measured at 410 K while light

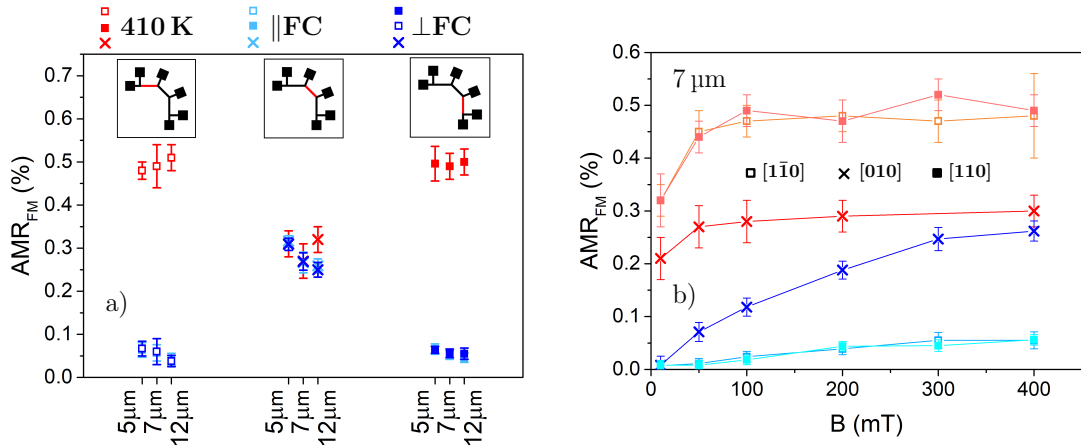


**Fig. 5.9:** a) Fitted  $AMR$  values for different segments of stripes with widths of  $5\ \mu\text{m}$ ,  $7\ \mu\text{m}$  and  $12\ \mu\text{m}$  at 410 K and at 300 K after field cooling in 400 mT magnetic field parallel and perpendicular to the 40-nm-thick FeRh stripe segment on an MgO substrate. b) Dependence of the fitted  $AMR$  on the magnetic field value used for measurement of the same stripe segments.

and dark blue are measured at 300 K after field cooling parallel and perpendicular to the stripe, respectively. These results suggest that the width of stripes does not play a role in the  $AMR$  value. The  $AMR$  value of the segments along  $[1\bar{1}0]$  and  $[110]$  in the high temperature state reaches a similar value of 0.5 % and in the low temperature state it decreases to approximately 0.05 %. However, in the diagonal segment oriented along the  $[010]$  direction, the  $AMR$  is around 0.3 % both in the high and low temperature state, although the FM content of the low temperature state is about 10 % of the stripe volume and most current is shunted through the AF phase, thus lowering the actual FM  $AMR$  value.

The dependence of  $AMR$  on the value of magnetic field applied during the measurement of different segments of the 7- $\mu\text{m}$ -wide stripe is shown in Fig. 5.9b). The  $AMR$  at 410 K (red curves) does not change significantly in the range from 50 to 400 mT but drops for the 10-mT measurement in all segments. On the other hand, at 300 K (blue curves) the  $AMR$  decreases continuously throughout the whole range of measured field showing that the magnetization is harder to orient in the direction of the field.

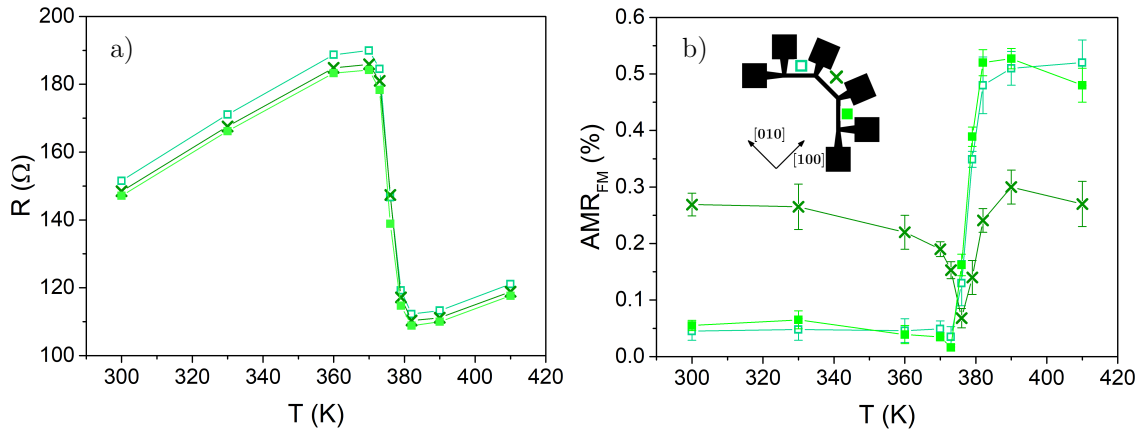


**Fig. 5.10:** Temperature dependence of a) the resistance and b) the FM  $AMR$  in the 7- $\mu\text{m}$ -wide and 40-nm-thick FeRh stripe segments on an MgO substrate.

To understand the intriguing behavior of  $AMR$  for low and high temperature state of different segments of the stripe structure, a deeper study of the effects happening throughout the phase transition was needed. Therefore the temperature dependence of  $R_{\perp}$  and of  $AMR$  for the three segments was measured and determined by the Matlab processing and is shown in Fig. 5.10a) and b), respectively. The slight shift of the resistance values of the three segments was probably caused by a small difference in their dimensions but the shape of the phase transition is the same for all of them. The value of  $AMR$  of the segments along  $[1\bar{1}0]$  and  $[110]$  directions is low at low temperatures and during the phase transition it rapidly increases. In contrast, the  $AMR$  of the segment along  $[010]$  is higher at low temperature then for the other two segments and decreases slowly when approaching the phase transition. In the

middle of the phase transition, the  $AMR$  is at its minimum and above this point it increases rapidly to the original value.

The angular dependences of a relative resistance change normalized to the minimum value of resistance in one cycle for different temperatures are plotted in Fig. 5.11a)-b) and Fig. 5.11c)-d) for the segments along  $[1\bar{1}0]$  and  $[010]$  directions, respectively. In the segment along  $[1\bar{1}0]$  the position of the maximum value changes at the end of the transition (Fig. 5.11b)). A slight position change of the resistance maximum can be seen in the segment along  $[010]$ , where a small rotation of the high resistance direction occurs in the case, where the  $AMR$  is the smallest in the middle of the transition (Fig. 5.11d)).

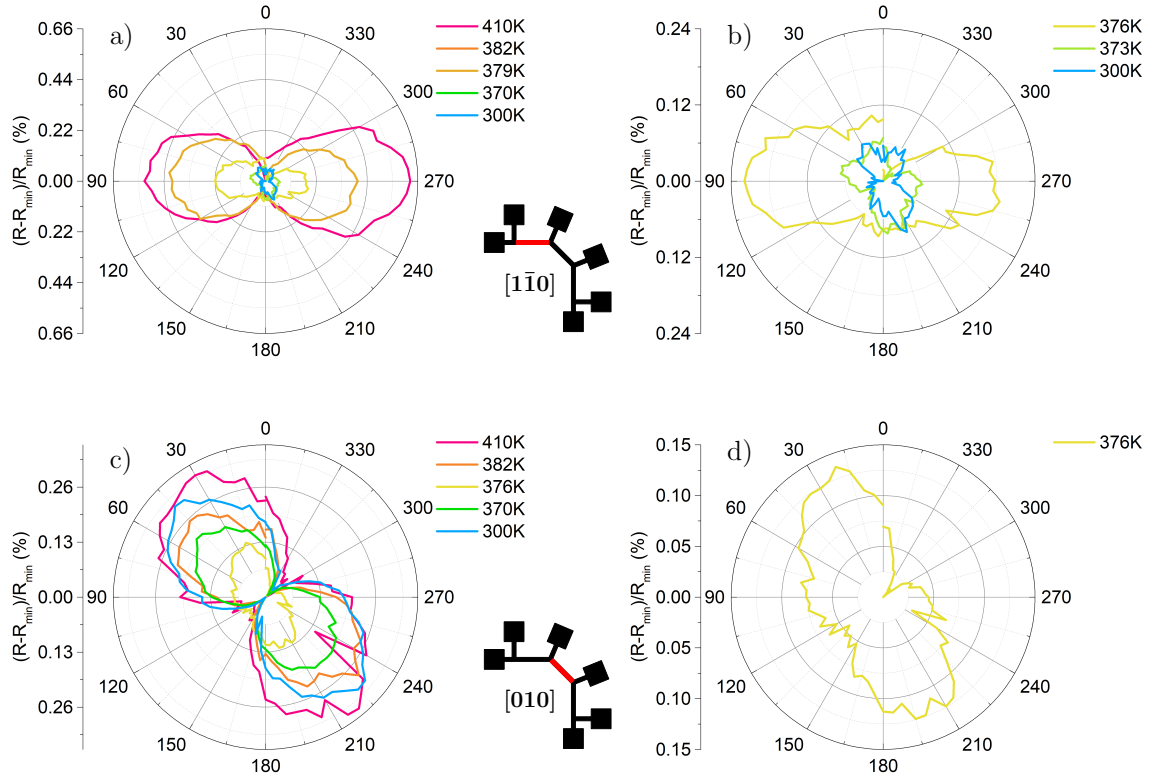


**Fig. 5.11:** Polar plots of  $AMR$  of the segments along a), b)  $[1\bar{1}0]$  and c), d)  $[010]$  direction of the 7- $\mu\text{m}$ -wide and 40-nm-thick FeRh stripe structure on an MgO substrate at different temperatures.

### 5.2.2 Angular dependence of $AMR$ - effect of stripe thickness

For comparison, The angular dependence of  $AMR$  was measured in FeRh stripes of 20-nm and 10-nm thickness. The structures were prepared only in the form of *Hall bars* that gives possibility to measure  $AMR$  only in the segment along the  $[1\bar{1}0]$  crystal direction.

Polar graphs of the two samples measured in a high and low temperature phase after field cooling in 400-mT magnetic field parallel to the stripes are plotted in

Fig. 5.12 and Fig. 5.13. The low temperature phase after perpendicular field cooling is not shown, as it looks the same as in the case of parallel field cooling. It could not be plotted in one graph, because the nominal value of resistance was changing for every measurement after the cooling no matter how the sample was cooled. This was caused by an incomplete phase transition at the low temperature, where the actual resistance reading is very sensitive to the exact temperature value.

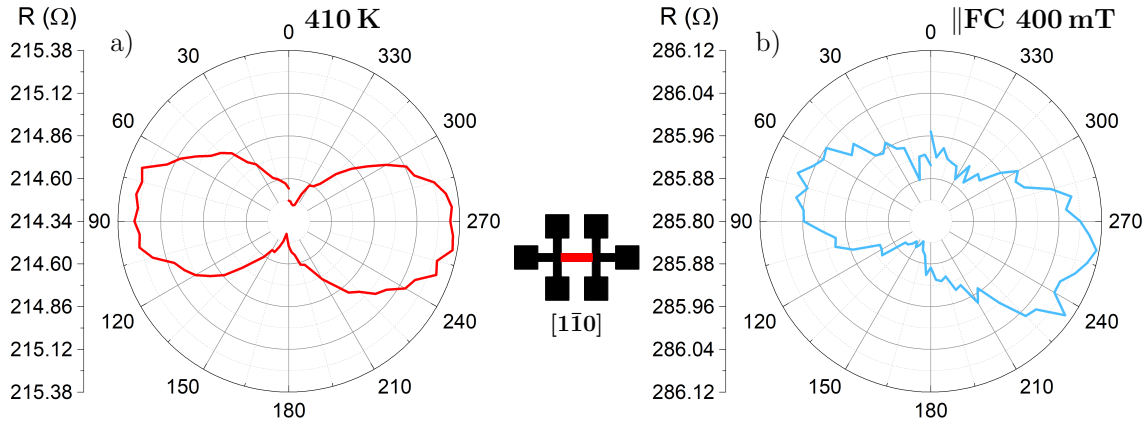


**Fig. 5.12:** Polar plot of angular dependence of resistance on the magnetization direction for the 20-nm-thick FeRh stripe on an MgO substrate oriented along  $[1\bar{1}0]$  crystal direction measured at a) 410 K and at b) 300 K after field cooling in 400 mT  $\parallel$ FC.

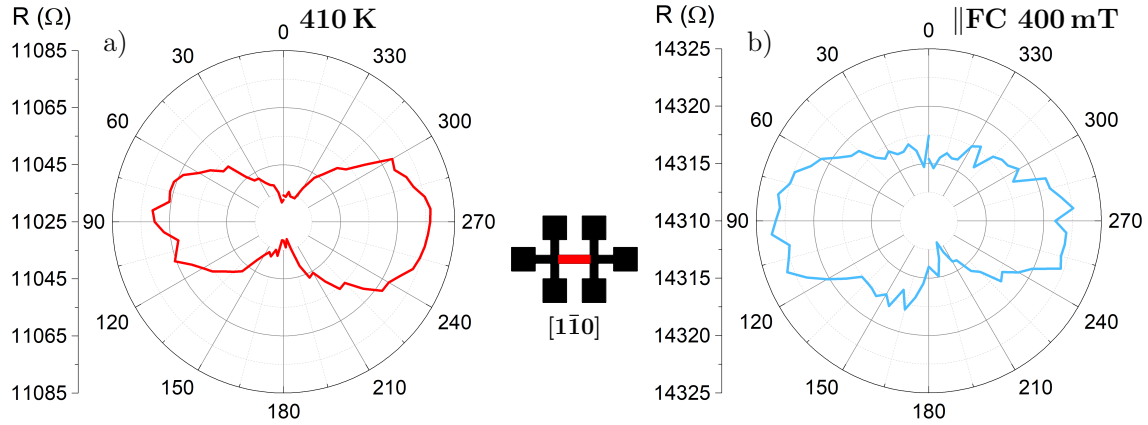


**Fig. 5.13:** Polar plot of angular dependence of resistance on the magnetization direction for the 10-nm-thick FeRh stripe on an MgO substrate oriented along  $[1\bar{1}0]$  crystal direction measured at a) 410 K and at b) 300 K after field cooling in 400 mT  $\parallel$ FC.

For both the 20-nm-thick and 10-nm-thick stripes, the shape of the polar graphs at high temperature (410 K) measured in 400-mT magnetic field, shows the same character as the corresponding stripe segment in the sample with 40-nm-thick



stripes and the resistance maximum is aligned along the stripe. However, the position of the resistance maximum of the low temperature phase changes with the stripe thickness. In the 40-nm-thick stripes, the maximum at low temperature is rotated by approximately  $75^\circ$  with respect to the high temperature phase, in the 20-nm-thick stripe it is rotated only by approximately  $15^\circ$  and in the 10-nm-thick stripe, the rotation is barely visible. The dependence of the *AMR* value in the high temperature phase and low temperature phase (for parallel and perpendicular field cooling) on the thickness of the stripes is plotted in Fig. 5.14. The *AMR* of the high temperature phase increases with the thickness while in the low temperature phase it decreases. Comparing the *AMR* related to the two field cooling protocols didn't show any significant differences.

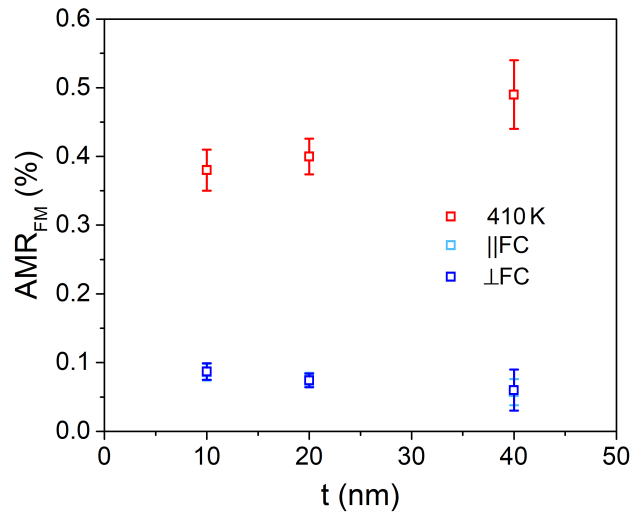


**Fig. 5.14:** Dependence of FM *AMR* at 410 K and 300 K on the thickness of FeRh stripes oriented along the  $[1\bar{1}0]$  crystallographic direction.

### 5.2.3 Angular dependence of *AMR* - effect of the W buffer layer

Two samples of FeRh layer prepared on MgO substrate with 10 nm thick tungsten buffer layer were patterned with stripe structures and used for *AMR* measurements. The data were processed in the way described in Chapter 4 to subtract the tungsten contribution to the resistance and obtain only the resistance of the FeRh stripe. The results presented further in the text are the processed data without the W contribution.

The 40-nm-thick FeRh layer on an MgO\W substrate was patterned with a 5- $\mu$ m-wide stripe structure where the three segments are oriented along different crystallographic directions ( $[1\bar{1}0]$ ,  $[010]$  and  $[110]$ ). We measured the angular dependence of resistance in the same manner as for the 40-nm-thick FeRh stripes on a pure MgO substrate. The polar plots of resistance in the high temperature phase of these three

segments are plotted in Fig. 5.15a)-c). The shape resembles the results obtained with the previous samples, where the maximum resistance is aligned with the orientation of stripes. The low temperature phase polar plots are not shown here, because the measured *AMR* values extracted from the polar plots of the low temperature state basically correspond to the noise level of the resistance measurement.

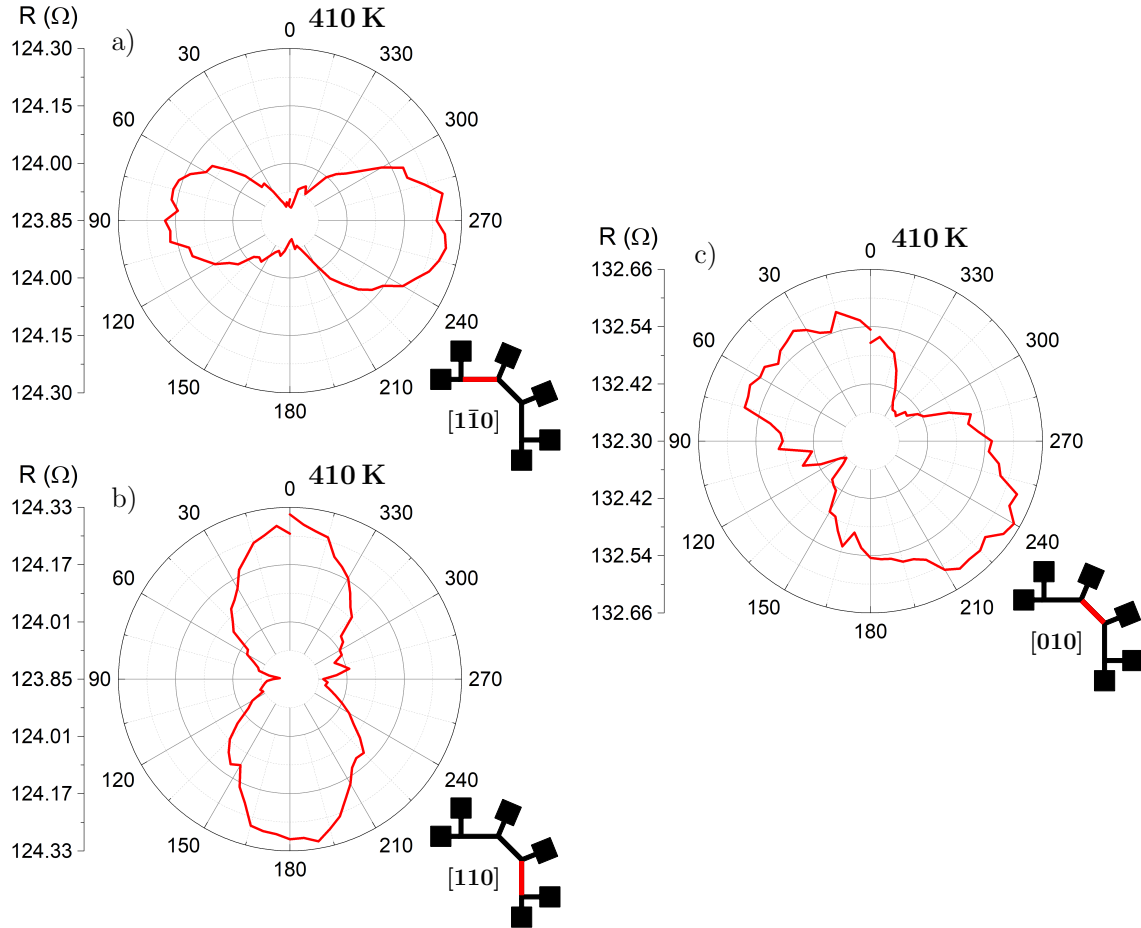


**Fig. 5.15:** Polar plot of angular dependence of the resistance on magnetization direction corresponding to the 40-nm-thick FeRh stripe on MgO\W oriented along a)  $[1\bar{1}0]$ , b)  $[110]$  and c)  $[010]$  crystal directions measured with 400-mT magnetic field at 410 K.

The processed *AMR* values of high and low temperature phase are plotted in Fig. 5.16a) for the three segments. Even though the value of resistance in the high temperature state is lower than in the previous samples on pure MgO, the segments along  $[1\bar{1}0]$  and  $[110]$  direction show similar behavior. However, even the segment oriented along the  $[010]$  direction does not show any *AMR* in the low temperature state, which is different from the same segment of FeRh grown directly on MgO. In Fig. 5.16b), the dependence of the *AMR* on the magnitude of the magnetic field is plotted for the high temperature phase. In all three segments, the magnetic field above 100 mT is sufficient to rotate the magnetization perpendicular to the stripe.



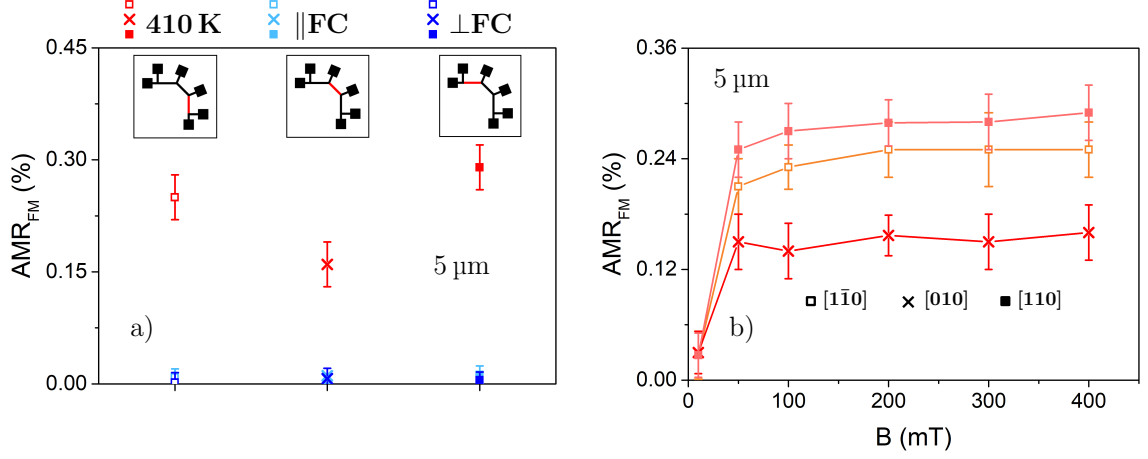


**Fig. 5.16:** a) Fitted  $AMR$  values for different segments of stripes with 5- $\mu\text{m}$  width at 410 K and at 300 K after field cooling in 400-mT magnetic field parallel and perpendicular to the 40-nm-thick FeRh stripe segment on MgO\W. b) Dependence of the fitted  $AMR$  on the magnetic field value used for measurement of the same stripe segments.

To map the  $AMR$  evolution during heating, several temperatures were chosen to characterize the  $AMR$  temperature dependence around the phase transition. The results plotted in Fig. 5.17 show that above the phase transition in both segments oriented along the  $[1\bar{1}0]$  and  $[010]$  directions, the  $AMR$  increases rapidly. Similarly to the plots in Fig. 5.16a) and b), the  $AMR$  of the segment along the  $[010]$  direction is significantly smaller than the  $AMR$  in the other two segments. However, the increase of  $AMR$  in this segment below the phase transition is not observed.

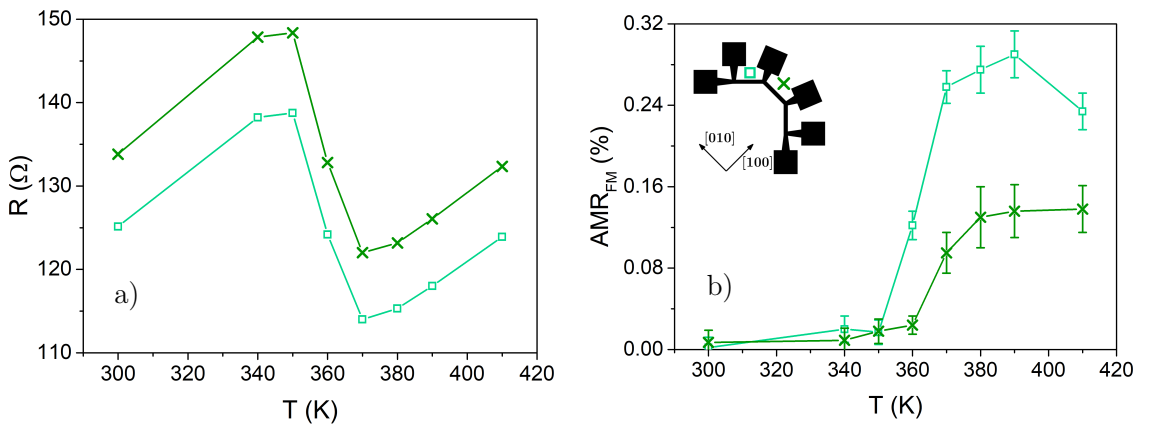


**Fig. 5.17:** Temperature dependence of a) the resistance and b) the FM  $AMR$  in the 5- $\mu\text{m}$ -wide and 40-nm-thick FeRh stripe segments on MgO\W.

Furthermore, the effect of stripe thickness is studied for the 20-nm-thick FeRh stripe on an MgO with a 10-nm-thick W buffer layer. The structures patterned into

a *Hall bar* with the measured segments along the  $[1\bar{1}0]$  crystallographic direction. The high and low temperature phase polar plots are displayed in Fig. 5.18. Although the high temperature polar graph shows behavior consistent with the previous results, the low temperature polar graph changes its symmetry. The maximum of the resistance lies well along the stripe which is different from the corresponding 20-nm-thick FeRh stripe on pure MgO where the maximum was slightly rotated. Additionally, in the direction perpendicular to the stripe, where a minimum is expected, the resistance slightly increases again.

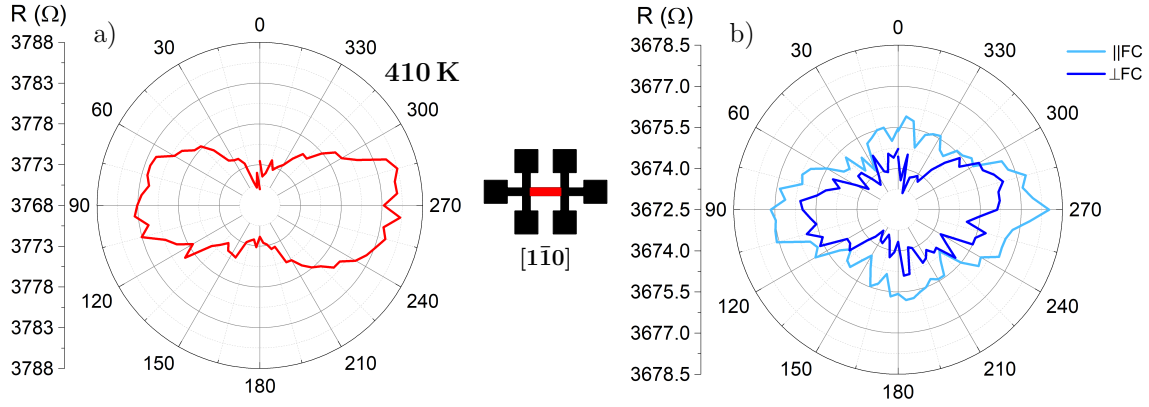


**Fig. 5.18:** Polar plot of angular dependence of resistance on the magnetization direction of the 20-nm-thick FeRh stripe on MgO\W oriented along the  $[1\bar{1}0]$  crystal direction measured at a) 410 K and at b) 300 K after field cooling in 400-mT magnetic field parallel and perpendicular to the stripe.

The temperature dependence of the *AMR* and resistance during heating is plotted in Fig. 5.19 and clearly follows a similar trend as the stripes oriented along the same directions in previous samples.

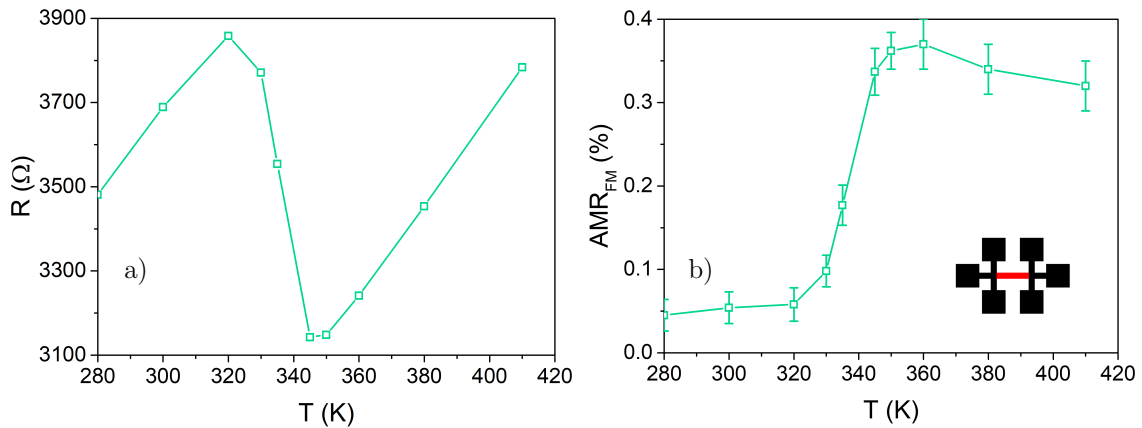


**Fig. 5.19:** Temperature dependence of a) the resistance and b) the FM *AMR* in 5- $\mu$ m wide and 20-nm-thick FeRh stripe segment along the  $[1\bar{1}0]$  direction on MgO\W.

The Fig. 5.20 shows dependence of  $AMR$  of low and high temperature phase on the thickness of the FeRh layer on an MgO substrate with a W buffer layer. The decrease of  $AMR$  in both phases is visible for thicker FeRh. Notably, the  $AMR$  is consistently lower than in the FeRh stripes on pure MgO.

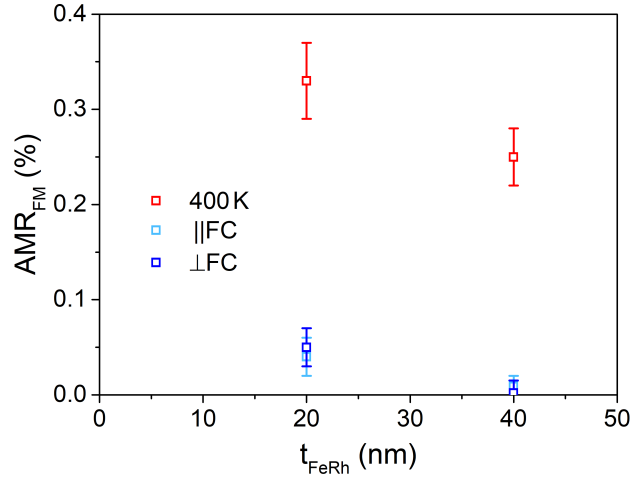


**Fig. 5.20:** Dependence of FM  $AMR$  at 410 K and 300 K on the FeRh thickness of measured stripes oriented along the  $[1\bar{1}0]$  crystallographic direction on MgO\W.

## 5.3 Discussion

### 5.3.1 AMR of the FM phase in the high temperature state

The results of AMR measurement in FeRh stripes presented in the previous section show that the 40-nm-thick FeRh stripes on an MgO substrate oriented along  $[1\bar{1}0]$  and  $[110]$  FeRh crystallographic directions exhibit  $AMR$  in the FM phase with the amplitude around 0.48 %. The width of the stripes does not seem to notably influence this value and the results are in a good agreement with 0.45 %  $AMR$  determined for a 100-nm-thick FeRh layer on MgO by M. Sharma [38]. The thinner stripes manifest a decreasing trend in the  $AMR$  value at high temperatures (Fig. 5.14). This effect might be explained by increased concentration of defects in thinner structures causing larger electron scattering and therefore influencing the  $AMR$  value.

The measurements of FeRh stripes on MgO with a W buffer layer show smaller FM  $AMR$  at high temperatures than those grown directly on MgO. The nature of this effect is not straightforward. One likely factor to influence the results could be the incorrect subtraction of W contribution to the resistance in stripes as the idealized arrangement of two parallel resistors is assumed, while, for example, the roughness of the interfaces could impair this simple model. Another explanation might be given by taking into account the strain caused by the substrate. The lattice mismatch of FeRh on W causes the in-plane tensile strain which is different

for FeRh on MgO, where FeRh is slightly compressed. Also the thickness of FeRh on the substrate is important because in thicker films, the strain caused by the substrate is less significant as the layer gets relaxed. This would explain the dependence of *AMR* on FeRh thickness. As the FeRh thickness on MgO increases, the compressive strain decreases and *AMR* gets to higher values. In the case of FeRh on a W buffer layer, this explanation suggests that the tensile strain is larger in thinner FeRh films and thus the corresponding *AMR* is higher.

Another effect observed in our measurements is that the FeRh stripes on MgO and also on MgO with a W buffer layer oriented along the [010] crystallographic direction in the high temperature state exhibit significantly lower *AMR* than the stripes rotated by  $45^\circ$  ( $[1\bar{1}0]$  and  $[110]$  directions). This could be caused by the anisotropic resistance along different crystallographic directions which could also modify the measured *AMR*.

### 5.3.2 *AMR* of the FM phase in the low temperature state

The behavior of *AMR* in the low temperature state changes significantly with the orientation of the segments and differs throughout the samples. The segments along  $[1\bar{1}0]$  and  $[110]$  directions exhibit generally small *AMR* (below 0.1 %). In thicker FeRh stripes on MgO, the reorientation of the *AMR* axis can be observed in these segments. If the magnetization is aligned with the applied field, the maximum of resistance should lie in the direction of the stripe like it is visible in all polar graphs for the high temperature state. However, in the low temperature state for 40-nm-thick FeRh stripes on MgO, the maximum is rotated by approximately  $75^\circ$  whereas in 20-nm-thick stripes the rotation is significantly lower (around  $15^\circ$ ) and in the 10-nm-thick stripe, no rotation is observed. Fig. 5.9b) highlights that the 400-mT magnetic field might not be sufficient to align magnetization in all directions. Additionally, the presence of some magnetocrystalline anisotropy in the stripes could result in a shift of the *AMR* maximum. The competition between the Zeeman energy and anisotropy energy could result in orienting the magnetization along the stripes for different magnetic field direction. In any case, the rotation by  $75^\circ$  is too large to be explained by this effect. Other explanation could be a change in sign of *AMR*, as it is not necessary for the higher resistance to correspond to the magnetization aligned with the current flow and the smaller resistance to the perpendicular arrangement, because in some materials the effect can be opposite [12]. However, the *AMR* in the high temperature state of FeRh exhibits common behavior and in the low temperature phase we measure again the remaining FM phase of FeRh, therefore we do not anticipate a significant change.

The aforementioned effect of *AMR* reorientation in the low temperature phase was not observed in FeRh stripes on a W buffer layer on MgO. In the 40-nm-thick FeRh, the *AMR* at low temperatures was so miniscule that it was not observable and in the 20-nm-thick FeRh the maximum was aligned along the stripe, similar to

the orientation observed for 20-nm-thick FeRh stripe on pure MgO.

The segment along  $[010]$  direction in 40-nm-thick FeRh on MgO exhibits no AMR reorientation in the low temperature phase but the *AMR* value was unexpectedly high as its value reached around 0.3 % which is comparable to the high temperature value of the same segment. During the phase transition, the *AMR* drops to almost 0.1 % but increases again at lower temperatures. The same effect is not observed for segments oriented along the  $[1\bar{1}0]$  and  $[110]$  directions, although the character of the phase transition is the same in all segments and the FM phase content should be the same even in the low temperature state.

To help clarify this behavior, measurements with Magneto-optical Kerr effect (MOKE) microscopy were carried out to examine the anisotropy in the FeRh stripes. The measurements in the high temperature phase show the preferential orientation of magnetization along  $[100]$  and  $[010]$  crystallographic directions of FeRh. For the low temperature state it was not possible to evaluate the results, because the MOKE is insensitive to the AF phase and because the residual FM phase is located at the buried interface with the MgO substrate which is outside the scope of MOKE microscopy as it is a surface sensitive method (approximately to 30 nm). The experiment confirms that at low temperature the FeRh is mostly in the AF phase in all three segments of the stripe structure but to understand what is happening at the bottom interface, further analysis is needed.

### 5.3.3 AMR of the AF phase

The AMR of the AF phase of FeRh should be manifested by different nominal resistance value of the resistance after field cooling with magnetic field oriented parallel and perpendicular to the stripe. According to the results shown in Fig 5.6c) and d), though, there is no difference in resistance for two different field cooling orientations.

The reason why the AF AMR is not noticeable in our samples may have two origins. One of the reasons might be the composition of FeRh. X. Marti showed in his work in 2014 that the *AMR* value of the AF phase, calculated for Rh-rich FeRh using the Kubo formula CPA-TB-LMTO formalism, strongly depends on the ratio of Fe and Rh atoms [3]. It reveals that for the ratio of 1:1 the *AMR* of AF phase tends to approach zero. Another reason might be that magnetic field of 400 mT applied during the field cooling might not be enough to affect the ordering of the AF phase during the phase transition. In personal consultation with X. Marti, he revealed that in their experiments, it was necessary to apply magnetic field of at least 1 T to establish the orientation of the AF spin axis properly.

Nevertheless, in T. Moriyama study of AF AMR in FeRh [41], they used 300-mT magnetic field during field cooling and they observed the *AMR* of the AF phase to be 0.011 % which is quite low compared to the value obtained by Marti (0.4 %). They explain this difference by the composition of their FeRh with the ratio of 1:1

which is similar to our case, but such low  $AMR$  is well below the detection limit of our setup.

The in-depth inspection of the AMR of the FeRh AF phase should thus be performed in higher magnetic fields which our present setup does not allow.

# CONCLUSION

This work is related to the study of magnetotransport properties of FeRh nanowires and stripes. FeRh undergoes phase transition from the antiferromagnetic (AF) to ferromagnetic (FM) state which can be induced by the action of temperature or magnetic field. The phase transition is manifested by an abrupt change in characteristic properties like magnetization, volume and a significant drop in resistivity. The main focus of this work is on the study of anisotropic magnetoresistance (AMR)s of the FM and AF phase in FeRh nano- and microstructures.

In Chapter 1, the basic quantities to describe a magnetic field in matter and the magnetic properties of materials are summarized. The description of FM and AF materials is included along with the definition of the AMR.

Chapter 2 introduces the FeRh alloy, its general properties and the phase transition characteristics. Several approaches to induce and modify the phase transition are summarized with the focus on the influence of magnetic field, elemental substitution, hydrostatic pressure and strain. At the end of this chapter, the electric transport properties of FeRh thin films and nanostructures are presented and the state-of-the-art of the AMR studies in FeRh in the FM and AF phases is reviewed.

Chapter 3 outlines the preparation processes of FeRh thin films and subsequent lithographic procedures for patterning films into microstructures for electric transport measurements.

Chapter 4 provides the description of characterization methods used in this work and their working principles. One of them is the new experimental setup which was developed to measure the angular dependence of resistance in stationary magnetic field. The processing of the measured resistance in FeRh stripes is presented at the end of this chapter.

In the final chapter, the results of AMR measurements in FeRh structures are presented and discussed. At the beginning, the AMR in nanowires is examined using the Lakeshore system where the magnetic field is applied along the in-plane hard axis direction and the resistance dependence on the magnitude of the field is measured. From these measurements it was concluded that higher magnetic field is needed to well define the magnetization in the hard axis direction and therefore wider structures with lower shape anisotropy field were chosen for further studies. As the setup did not allow rotation of samples without disconnecting the electric contacts, it was not possible to well define both the high-resistance and low-resistance magnetization directions at the same time. For the same reason, the measurement of AMR of the AF phase was not possible. Therefore, a new setup for measurement of AMR by rotating the sample in stationary in-plane magnetic field was developed.

Using this setup, we successfully determined the *AMR* value of the FM phase of FeRh in the high temperature phase and the obtained results are well consistent with literature. We further found that the *AMR* value of the FM phase in the high temperature state depends on the orientation of the stripes with respect to the

crystallographic directions.

Interesting unexpected behavior of the  $AMR$  of the FM phase was discovered in the low temperature phase. In the 40-nm-thick FeRh stripe on MgO oriented along  $[010]$  FeRh crystallographic direction, an unexpected increase of the FM  $AMR$  was observed. This behavior was not observed in the corresponding stripe on MgO/W substrate. In the stripes along  $[1\bar{1}0]$  and  $[110]$  directions, the expected decrease of  $AMR$  was observed, although a significant rotation of the maximum resistance direction of the FeRh FM phase was observed in thicker stripes.

This unexpected behavior was not possible to fully explain within this work and will require a deeper study of the magnetocrystalline anisotropy and crystalline anisotropy of resistance in the system.

The AMR of the AF phase was not successfully measured as the applied magnetic field during field cooling was probably too low to sufficiently establish the orientation of the AF spin axis, or the measured AMR was too low to detect with the current setup.



# BIBLIOGRAPHY

- [1] Fallot, M. and Hocart, R. *Sur l'apparition du ferromagnétisme par élévation de température dans des alliages de fer et de rhodium*. Revue Scientifique, vol. 77, pp. 498-499, 1939.
- [2] Thiele, J.-U.; Maat, S. and Fullerton, E. E. *FeRh/FePt exchange spring films for thermally assisted magnetic recording media*, Applied Physics Letters, vol. 82, pp. 2859, 2003.
- [3] Marti, X. et al. *Room-temperature antiferromagnetic memory resistor*, Nature Materials, vol. 13, no. 4, pp. 367-374, 2014.
- [4] Annaorazov, M. P. et al. *Alloys of the Fe-Rh system as a new class of working material for magnetic refrigerators*, Cryogenics, vol. 32, no. 10, pp. 867-872, 1992.
- [5] Stern-Taulats, E. et al. *Barocaloric and magnetocaloric effects in  $Fe_{49}Rh_{51}$* , Physical Review B, vol. 89, no. 21, pp. 214105, 2014.
- [6] Coey, J. M. *Magnetism and Magnetic Materials*. Cambridge University Press, 2010.
- [7] Vaňatka, M. *Spin vortex states in magnetostatically coupled magnetic nanodisks*. Brno University of Technology, Faculty of Mechanical Engineering, 2015. 59 p., Supervised by Ing. Michal Urbánek, Ph.D.
- [8] Stöhr, J.; Siegmann, H. *Magnetism: From Fundamentals to Nanoscale Dynamics*. Springer, 2006.
- [9] Uhlíř, V. *Current Induced Magnetization Dynamics in Nanostructures*. Brno University of Technology, Faculty of Mechanical Engineering, 2010. 239 p., Supervised by prof. RNDr. Tomáš Šikola, CSc.
- [10] Blundell, S.; and Thouless, D. *Magnetism in Condensed Matter*, Oxford university press, 2001.
- [11] Sedlák, B.; and Štoll, I. *Elektrina a magnetismus*, Academia, 2002.
- [12] McGuire, T. R. and Potter, R. I. *Anisotropic Magnetoresistance in Ferromagnetic 3d Alloys*, IEEE Transactions on Magnetism, vol. 11, pp. 1018, 1976.
- [13] Bertaut, E.; de Bergevin, F. and Roullet, G. *Neutron Diffraction Study of  $Fe_{0.4}Rh_{0.53}$* . Comptes Rendus de l'Académie des Sciences, vol. 256, pp. 1688-1691, 1963.
- [14] Shirane, G.; Nathans, R. and Chen, C. W. *Magnetic Moments and Unpaired Spin Densities in the Fe-Rh Alloys*, Physical Review, vol. 134, pp. A1547-A1553, 1964.
- [15] Zakharov, A. I. et al. *Magnetic and magnetoelastic properties of a metamagnetic iron-rhodium alloy*, Soviet Physics JETP, 1964.
- [16] Wayne, R. C. *Pressure Dependence of the Magnetic Transitions in Fe-Rh Alloys*, Physical Review, vol. 170, pp. 523-527, 1968.

- [17] Algarabel, P. A. et al. *Giant room-temperature magnetoresistance in the FeRh alloy*, Applied Physics Letters, vol. 66, no. 22, pp. 3061–3063, 1995.
- [18] van Driel, J. et al. *Compositional dependence of the giant magnetoresistance in  $Fe_xRh_{1-x}$  thin films*, Journal of Applied Physics, vol. 85, no. 2, pp. 1026–1036, 1999.
- [19] Swartzendruber, L. J. *The Fe-Rh (Iron-Rhodium) System*, Bulletin of Alloy Phase Diagrams, vol. 5, no. 5, pp. 456–462, 1984.
- [20] Kouvel, J. S. *Unusual Nature of the Abrupt Magnetic Transition in FeRh and Its Pseudobinary Variants*, Journal of Applied Physics, vol. 37, no. 3, pp. 1257–1258, 1966.
- [21] Barua, R.; Jiménez-Villacorta, F. and Lewis, L. H. *Predicting magnetostructural trends in FeRh-based ternary systems*, Applied Physics Letters, vol. 103, no. 10, 2013.
- [22] Maat, S.; Thiele, J.-U.; Fullerton, E.E. *Temperature and field hysteresis of the antiferromagnetic-to-ferromagnetic phase transition in epitaxial FeRh films*, Physical Review B, vol. 72, no. 21, pp. 214432, 2005.
- [23] Kubaschewski, O. *IRON-Binary Phase Diagrams*, Springer Berlin Heidelberg, 1982.
- [24] Inoue, S.; Ko, H. Y. Y. and Suzuki, T. *Magnetic Properties of Single-Crystalline FeRh Alloy Thin Films*, IEEE Transactions on Magnetics, vol. 44, no. 11, pp. 2875–2878, 2008.
- [25] Rosenberg, M. et al. *A Mössbauer spectroscopy and magnetic study of FeRh* Journal of Magnetism and Magnetic Materials, vol. 177-181, 1998.
- [26] Jaskowiec, J. *Mikroskopie magnetických sil a transportní vlastnosti metamagnetických nanostruktur*, Brno University of Technology, Faculty of Mechanical Engineering, 2017. 47 p., Supervised by Ing. Vojtěch Uhlíř Ph.D.
- [27] Papon, P.; Leblond, J. and Meijer, P. H. E. *The Physics of Phase Transitions: Concepts and Applications*, Springer Berlin Heidelberg, 2007.
- [28] Ceballos, A. et al. *Effect of strain and thickness on the transition temperature of epitaxial FeRh thin-films*, Applied Physics Letter, vol. 111, no. 17, pp. 172401, 2017.
- [29] Bordel, C. et al. *Fe Spin Reorientation across the Metamagnetic Transition on Strained FeRh Thin Films*, Physical Review Letters, vol. 209, no. 11, 2012.
- [30] Cherifi, R. O. et al. *Electric-field control of magnetic order above room temperature*, Nature Materials, vol. 13, no. 4, pp. 345-351, 2014.
- [31] Lee, Y. et al. *Large resistivity modulation in mixed-phase metallic systems*, Nature Communications, vol. 6, no. 1, 2015.
- [32] Davey, W. P. *The Lattice Parameter and Density of Pure Tungsten*, Physical Review, vol. 26, no. 6, pp. 736-738, 1925.
- [33] Lee, J.-S. et al. *Electronic structure and magnetic properties of epitaxial FeRh(001) ultrathin films on W(100)*, Physical Review B, vol. 82, no. 22, pp. 224410, 2010.

- [34] Drózdź, P. et al. *Switching of Co Magnetization Driven by Antiferromagnetic-Ferromagnetic Phase Transition of FeRh Alloy in Co/FeRh Bilayers*, Physical Review Applied, vol. 9, no. 3, 2018.
- [35] Witte, R. et al. *Tailoring magnetic frustration in strained epitaxial FeRh films*, Physical Review B, volume 93, no. 10, 2016.
- [36] Lewis, L.H. et al. *Coupled magnetic, structural, and electronic phase transitions in FeRh*, Journal of Physics D: Applied Physics, vol. 49, no. 32, pp. 323002, 2016.
- [37] Kouvel, J. S. and Hartelius, C. C. *Anomalous Magnetic Moments and Transformations in the Ordered Alloy FeRh*, Journal of Applied Physics, vol.33, no. 3, pp. 1343-1344, 1962.
- [38] Sharma, M. et al. *Magnetotransport properties of epitaxial MgO(001)/FeRh films across the antiferromagnet to ferromagnet transition*, Journal of Applied Physics, vol. 109, no. 8, pp. 083913, 2011.
- [39] Uhlíř, V.; Arregi, J. A. and Fullerton, E. E. *Colossal magnetic phase transition asymmetry in mesoscale FeRh stripes*, Nature Communications, vol. 7, pp. 13113, 2016.
- [40] Fan, R. et al. *Ferromagnetism at the interfaces of antiferromagnetic FeRh epilayers*, Physical Review B, vol. 82, no. 18, 2010.
- [41] Moriyama, T. et al. *Sequential write-read operations in FeRh antiferromagnetic memory*, Applied Physics Letters, vol. 107, no. 12, pp. 122403, 2015.
- [42] Lommel, J.M. *Magnetic and Electrical Properties of FeRh Thin Films*, Journal of Applied Physics, vol. 37, no. 3, pp. 1483, 1966.
- [43] Gatzert, H. H.; Saile, V.; Leuthold, J. *Micro and Nano Fabrication*, Springer, 2014.
- [44] Vossen, J. L. and Kern, V. *Thin film processes II*, Boston: Academic Press, 1991.
- [45] Thiele, J.-U. et al. *Magnetic and Structural Properties of FePt-FeRh Exchange Spring Films for Thermally Assisted Magnetic Recording Media*, IEEE Transactions on Magnetics, vol. 40, no. 4, pp. 2537-2542, 2004.
- [46] Dushman, S. *Scientific foundations of vacuum technique*, New York: Wiley, 1962.
- [47] Pressacco, F. et al. *Stable room-temperature ferromagnetic phase at the FeRh(100) surface*, Scientific Reports, vol. 6, no. 1, 2016.